

The cosmological analysis of X-ray cluster surveys: II- Application of the CR-HR method to the XMM archive

N. Clerc^{1*}, T. Sadibekova¹, M. Pierre¹, F. Pacaud², J.-P. Le Fèvre³, C. Adami⁴,
B. Altieri⁵, I. Valtchanov⁵

¹Laboratoire AIM, CEA/DSM/IRFU/SAP, CEA Saclay, 91191 Gif-sur-Yvette, France.

²Argelander-Institut für Astronomie, University of Bonn, Auf dem Hügel 71, 53121 Bonn, Germany.

³CEA/DSM/IRFU/SEDI, CEA Saclay, 91191 Gif-sur-Yvette, France.

⁴LAM, OAMP, Université Aix-Marseille & CNRS, 38 rue Frédéric Joliot-Curie, 13388 Marseille 13 Cedex, France.

⁵ESAC, Villafranca del Castillo, Spain.

Accepted 2012 April 20. Received 2012 March 28; in original form 2011 September 20

ABSTRACT

We have processed 2774 high-galactic observations from the XMM archive (as of May 2010) and extracted a serendipitous catalogue of some 850 clusters of galaxies based on purely X-ray criteria, following the methodology developed for the XMM-LSS survey. Restricting the sample to the highest signal-to-noise objects (347 clusters), we perform a cosmological analysis using the X-ray information only. The analysis consists in the modelling of the observed colour-magnitude (CR-HR) diagram constructed from cluster instrumental count-rates measured in the [0.5-2], [1-2] and [0.5-1] keV bands. A MCMC procedure simultaneously fits the cosmological parameters, the evolution of the cluster scaling laws and the selection effects.

Our results are consistent with the σ_8 and Ω_m values obtained by WMAP-5 and point toward a negative evolution of the cluster scaling relations with respect to the self-similar expectation. We are further able to constrain the cluster fractional radius $x_{c,0} = r_c/R_{500c}$, to $x_{c,0} = 0.24 \pm 0.04$. This study stresses again the critical role of selection effects in deriving cluster scaling relations, even in the local universe. Finally, we show that CR-HR method applied to the eRosita all-sky survey - provided that cluster photometric redshifts are available - will enable the determination of the equation of state of the dark energy at the level of the DETF stage IV predictions; simultaneously, the evolution of the cluster scaling-relations will be unambiguously determined.

The XMM CCluster Archive Super Survey (XCLASS) serendipitous cluster catalogue is available online at: <http://xmm-lss.in2p3.fr:8080/l4sdb/>.

Key words: Cosmology: observations – Galaxies: clusters: general – X-rays: galaxies: clusters – Methods: observational – Catalogues

1 INTRODUCTION

Clusters of galaxies, the most massive bound objects in the universe, are the direct products of the growth of cosmic structures. Using cluster samples in cosmological analyses requires not only to span a large range of redshifts and masses. It is also mandatory to precisely understand how those objects have been selected and how the selection is related to the cosmological distribution of dark matter haloes, the only quantity handled by the theory. Indeed, understanding selection processes turned out to be one of the

main challenges of today's cluster cosmology and is intimately related to our ability to adequately determine cluster scaling-relations along with the associated dispersion. In this respect, X-ray surveys are potentially extremely powerful, given that the X-ray properties of the cluster population can be derived from *ab initio* models. Substantial efforts have been devoted to assemble statistically significant cluster samples with the past generation of X-ray observatories: (e.g. Scharf et al. 1997; Vikhlinin et al. 1998a; Jones & Forman 1999; Böhringer et al. 2000; Borgani et al. 2001; Böhringer et al. 2004; Burenin et al. 2007). Ten years ago, XMM opened a new era in cluster surveys, allowing us to access and to characterise clusters, much fainter than enabled by e.g., ROSAT. Nowadays, cluster serendip-

* Present e-mail: nclerc@mpe.mpg.de (MPE/Garching)

itous searches in the XMM archive arouse a growing interest thanks to the wealth of pointed observations, publicly available : The XCS survey (Romer et al. 2001), launched a decade ago is now delivering its first X-ray selected catalogues of clusters (Lloyd-Davies et al. 2011; Mehrrens et al. 2011). Several other projects are being conducted such as SExclass (Kolokotronis et al. 2006) and combined searches with Chandra archival data (Peterson et al. 2009) or SDSS optical data (Takey, Schwöpe, & Lamer 2011).

This paper is the second of a series describing a novel approach to the cosmological interpretation of cluster number counts in X-ray cluster surveys. The first paper (Clerc et al. 2011, hereafter paper I) investigated the constraining power of a method based on the analysis of instrumental X-ray observables, namely a count-rate (CR) and a hardness-ratio (HR) in well defined X-ray bands. The combination of the two quantities was shown to reliably describe the surveyed cluster population: the corresponding CR-HR statistical distribution, which is analogous to a colour-magnitude diagram, can be fully predicted by an *ab initio* modeling involving the cosmology, cluster scaling-relations, the survey selection effects along with the XMM instrumental response. In this paper, we present an independent analysis of 2774 high-galactic latitude observations from the XMM archive having effective exposure times of 10 and 20 ks. Following a selection procedure adapted from the XMM-LSS survey (Pierre et al. 2007), we detect 845 C1 galaxy clusters (Pacaud et al. 2007), hence constituting the X-CLASS catalogue (XMM Cluster Archive Super Survey). We apply the CR-HR method to a subsample of 347 clusters selected for their high signal-to-noise ratio over an effective geometrical area of 90 sq.deg. We devote special care to the count-rate measurements and to the derivation of the selection function associated to this heterogeneous archival data.

The structure of this paper is as follows. We first present the steps leading to the creation of the X-CLASS cluster sample (Sect. 2). In a second part (Sect. 3) we describe the derivation of the survey selection function and how we account for the presence of pointed clusters in the sample. In Sect. 4 and 5 we present the results of the analysis of the CR-HR distribution. We discuss our results in Sect. 6 and present some cosmological predictions for the eRosita all-sky survey. Summary and conclusion are gathered in Sect. 7.

2 THE X-CLASS CATALOGUE

The XMM CLuster Archive Super Survey (X-CLASS) is based on the analysis of archival observations from the XMM-Newton observatory. It is intended to provide a sample of several hundreds of clusters suitable for cosmological studies. In this section, we describe the selection of the original data and the adopted methodology for detecting and characterizing galaxy clusters.

2.1 Pre-selection of the XMM archival data

As of May, 26th 2010, 7716 individual observations were listed in the XMM Science Archive system (Arviset et al. 2003). Out of these, we retrieved 2774 observations selected as follows:

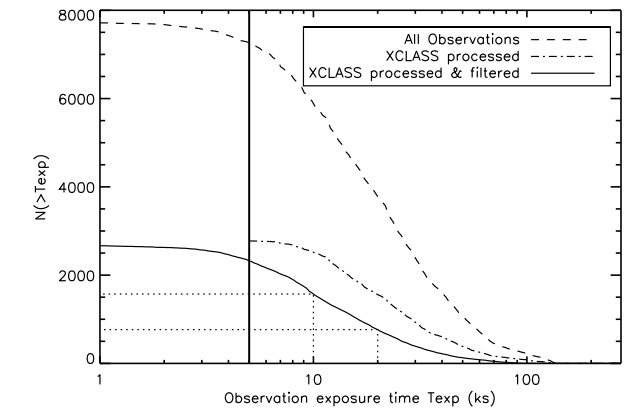


Figure 1. Cumulative exposure distribution of the XMM archival observations. *Dashed line*: nominal exposure time for all 7716 observations. *Dot-dashed line*: nominal exposure time for the 2774 retrieved observations. *Plain line*: effective “clean” exposure time after processing and background flare removal.

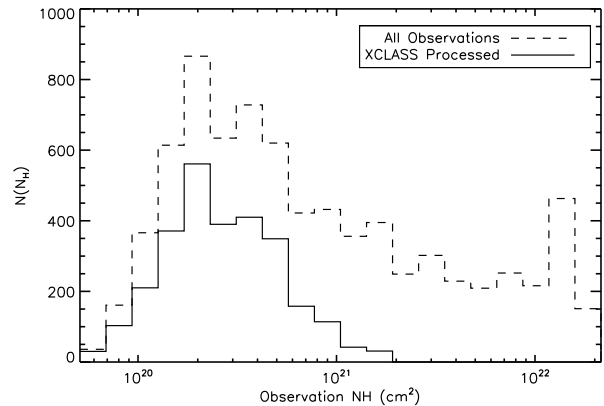


Figure 2. Distribution of hydrogen column densities, (*dashed line*: for the 7716 XMM archival observations, (*plain line*: for the 2774 pre-processed observations).

- (i) pointing center at high galactic latitude ($|b| \geq 20$ deg) to minimize the effect of galactic absorption,
- (ii) total exposure time greater than 5 ks,
- (iii) all three detectors (MOS1, MOS2 and PN) in imaging mode and at least one of them in Full Frame mode,
- (iv) pointing center not closer than 5 deg to the Small and Large Magellanic Clouds, and 2 deg away from M31,
- (v) public data (as of May, 26th 2010)

This selection contains in particular 92 observations from the 10 sq.deg. XMM-LSS survey (Pierre et al. 2007). Figure 1 presents the statistics of the exposure time distributions. Figure 2 shows the distribution of hydrogen column density (N_H) on the corresponding lines of sight. Column densities values were obtained through the Leiden/Argentine/Bonn N_H maps (Kalberla et al. 2005). Processed pointings show a median N_H of $\sim 3.10^{20} \text{ cm}^{-2}$ and very few of them lie in regions above 10^{21} cm^{-2} . We display on Fig. 3 the sky distribution of the processed observations.

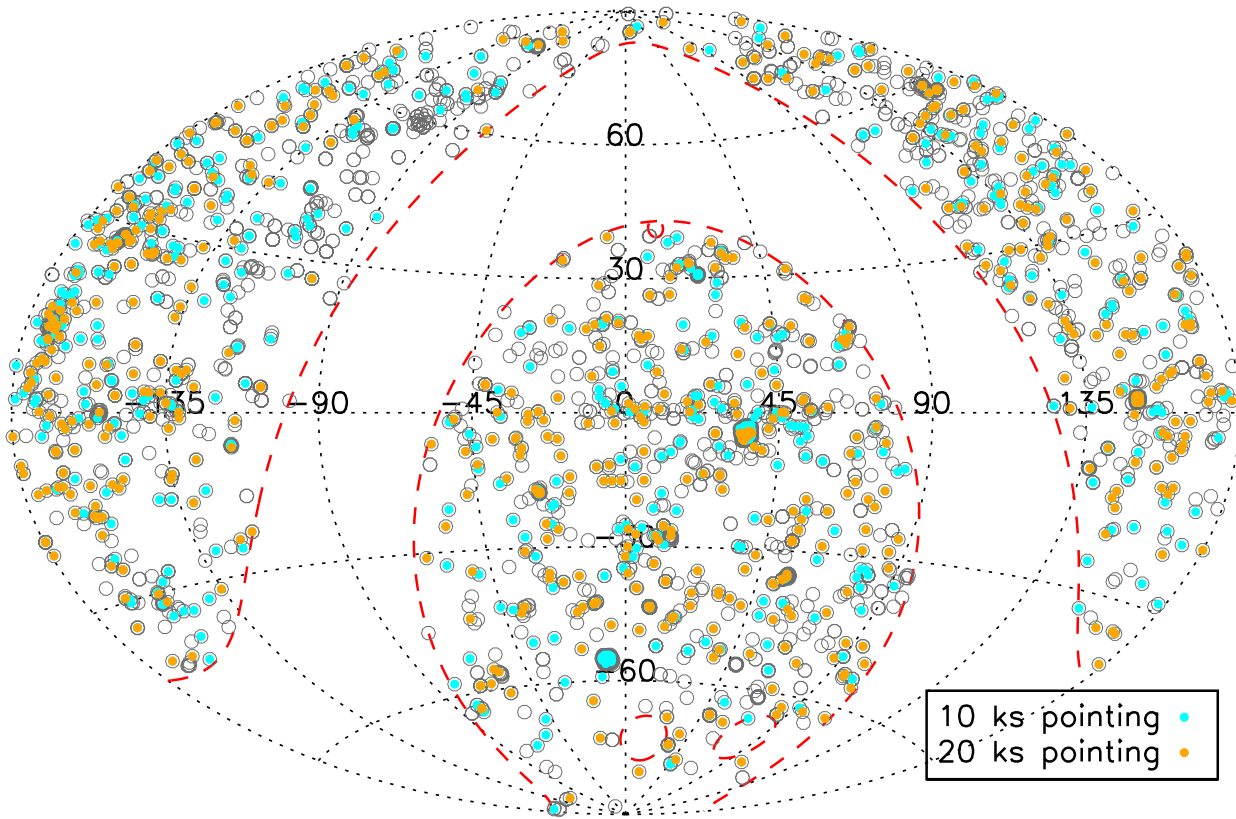


Figure 3. Sky location of the 2774 pre-processed XMM observations (equatorial coordinates). Observations shorter than 10 ks (open circles) were not considered for the X-CLASS catalogue. The other pointings have been truncated to 10 ks (blue points) and, if possible, to 20 ks (gold points). Note that, by construction, a gold point (20 ks pointing) always has a 10 ks counterpart. The circle size is not representative of the XMM field of view (~ 30 arcmin diameter).

2.2 Data processing and cluster detection

2.2.1 Processing steps

The individual Observation Data Files (ODF) pertaining to each observation were retrieved via the ESA Archive Inter-Operability system (XSA¹). Our processing is entirely based on the XMM-LSS pipeline (Pacaud et al. 2006) which main steps are summarized below.

(i) Event lists are generated using XMM-SAS tasks **emproc** and **epproc** and filtered from proton and solar flares. This is achieved by creating the high energy events light curves (12 – 14 keV for MOS and 10 – 12 keV for PN) and flagging out periods of high event rates (rates greater than 3σ above the mean observation count-rate). Although adequate for removing short periods of high flares, this procedure may provide unsatisfactory results for observations having a high mean particle background. The overall quality of each observation was then subsequently inspected by eye, and some observations discarded (Sect. 2.3).

(ii) Clusters detected with XMM exposure times of ~ 10 –20 ks constitute the most relevant population for cosmolog-

ical studies (Pierre et al. 2007, 2011); such exposure times are well above the XMM confusion limit. Further, the selection function of a survey consisting of homogeneous exposures is easier to handle. Using the *good time intervals* (GTI) resulting from the pre-processing, we thus build 10 ks and 20 ks “chunks” (now denominated “pointings”) from the original exposures, starting at the beginning of the observation. From each observation 0, 1 or 2 *pointings* are extracted, each pointing having exactly a 10 or 20 ks exposure time on the three detectors. The case of “0 pointing” occurs if one or more detector is insufficiently exposed, which corresponds to highly flared or problematic observations. Such observations are discarded from the analysis, and the total number of pointings entering the source detection process is 2409 (Table 1). We display in Fig. 3 the sky location of all pointings having a duration of exactly 10 or 20 ks and that subsequently undergo the source detection process. The archival GTI time used for cluster detection amounts thus to 24 Ms, over the 40 Ms GTI time available in total. In addition to these chunks, we construct a “full exposure” pointing containing the maximal GTI time from each observation, which will be used to obtain high signal-to-noise flux measurements for the detected clusters (Sect. 2.4).

(iii) For each observation, three images are created in

¹ <http://xmm.esac.esa.int/xsa/>

Table 1. Number of XMM archival observations handled for the present study. First line, all available observations. Second line, retrieved observations. Third line, number of usable observations after event filtering. Last line, final number of retained observations after discarding pathological cases (see. Fig. 8)

XMM observations (May, 26th 2010)	7716
Observations retrieved from the XSA	2774
Pointings "chunks" 10 + 20 ks	2409 (1588 + 821)
Pointings entering the cosmological analysis	1992 (1294 + 698)

the $[0.5 - 2]$ keV band, for the three EPIC detectors, which are in turn co-added. The resulting image is subsequently filtered in the wavelet space, assuming a Poisson noise model (`mr_filter`, Starck, Murtagh, & Bijaoui 1998; Valtchanov, Pierre, & Gastaud 2001), and sources are extracted running SExtractor (Bertin & Arnouts 1996) over the filtered image. Only sources detected within the inner 13 arcmin radius FoV are considered in the subsequent analysis.

(iv) Each detected source is further characterized by a maximum likelihood profile fitting procedure (XAMIN, Pacaud et al. (2006)). Two source models are tested on each detection: (1) a point-like model using the analytical PSF from the XMM calibration database, with the position held at the SExtractor output value, thus allowing two parameters to vary (the source count-rates on the MOS and PN detectors); and (2) a β -model, convolved by the PSF, with five free parameters ((X,Y) position, core radius extent and MOS and PN count-rates). A uniform background is added, whose level is such that the total number of photons in the data equals that of the modelled source plus background. We use the C-statistic (Cash 1979) for quantifying the likelihood of the fits and, finally, discriminating between the two types of sources.

This procedure, when coupled to a representative set of simulations, readily enables the selection of sub-samples of X-ray extended sources with well characterised levels of completeness and contamination. It is thus perfectly suited to the analysis of large X-ray data sets such as the XMM archive. We note, however, that the XAMIN pipeline was originally designed to detect and discriminate between point-like and extended sources in the XMM-LSS "empty" cosmological fields (Pierre et al. 2007); consequently, because of the variety of astronomical objects present in the XMM archive (nearby galaxies, substructures in clusters, planets...) a subsequent human screening is necessary (see Sect. 2.3) in order to remove mis-interpreted detections.

2.2.2 Output parameters and source characteristics

The procedures described above allow us to assign to each detected source a set of parameters characterising its properties: position on the detector, off-axis distance, sky coordinates, count-rates in various energy bands, plus three numbers related to the chosen fitting algorithm; (a) the detection likelihood (DET_ML) gives the significance of the detection as compared to a pure background fluctuation; (b) the angular extent (EXT) is the apparent core radius of the best-fit β -model; (c) the extent statistic (EXT_LIKE) compares the significances of the 'extended model' and the

'point-like model' and is thus called the source Extent Likelihood. These parameters can be easily related to the simulations intended to assess the survey selection function (see Sect. 3). Because of their relevance, these values are listed in the final cluster catalogue (App. A).

Following (Pacaud et al. 2006), we denote by "C1", sources characterised by `EXT_LIKE` > 33 and `EXT` > 5 arcsec : this corresponds to a sample of extended sources having a very low level of contamination by misclassified point-sources. We further show in Sect. 3 that this parameter combination can be applied regardless of the pointing intrinsic properties. Fig. 4 displays the pipeline detections over one XMM archival pointing (ObsID: 0403072201), containing three C1 candidates and ~ 60 point-like sources, most of them being AGNs.

2.3 Catalogue construction

2.3.1 Removal of duplicates

Only the high-quality C1 clusters are inserted into the final catalogue (App. A). Because of the multiple overlaps between the archival observations, several sources are detected in more than one pointing. In particular, if an observation has been split in two pointings (10 and 20 ks), almost all sources detected on the 10 ks pointing are also found on the deeper one (26 over the 845 extended detections were not in this case, most of them being close to the detection limit and four being nearby, bright clusters with a very peaked profile, mis-classified as point-sources). Furthermore, because of the presence of the CCD gaps and/or of multiple maxima in the emission of widely extended sources, multiple detections of the same object occurred.

We first associated sources closer than 20 arcsec to each other. To decide which of the two sources has to be included in the final catalogue, we applied the following rules: If the two sources are on different pointings, the one lying on the deeper pointing prevails. If both detection lie on the same pointing or on different pointings having the same exposure time, the source with the lowest Extent Likelihood is discarded. Each association was controlled by eye to avoid the matching of close, unrelated sources (e.g. a cluster and a background AGN). Note that positional differences of a few tens of arcsec are possible for extended sources located at the edge of the FoV, mainly because part of the emission is missing and because of the distorted shape of the PSF. This procedure was thus repeated with larger correlation radii, until each catalogue entry was related to a unique source.

2.3.2 Data screening and final selection

All remaining entries underwent a detailed screening based on optical data. For each putative cluster, we retrieved images from the Digitized Sky Survey (DSS) POSS-II on which we overlaid the X-ray contours. This step was mainly intended to remove extended sources, not relevant for our cluster catalogue: very large nearby clusters, halos of nearby galaxies, planets, unresolved double point-sources, and, possibly, saturated point-sources. For this purpose, the DSS images are sufficient. During this process each source was assigned a quality flag by two astronomers independently;

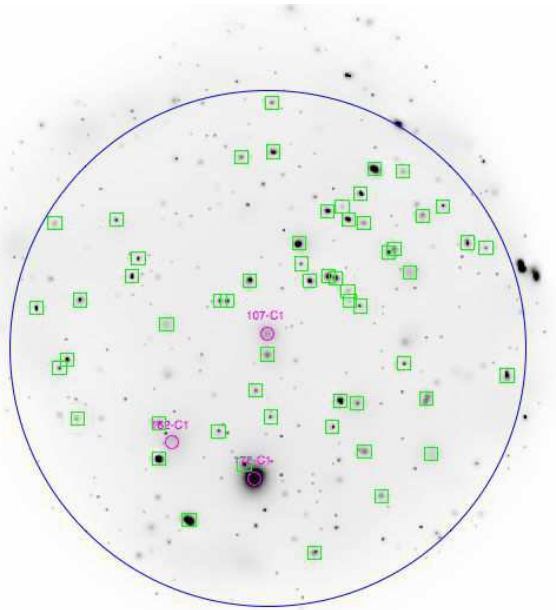


Figure 4. Example of wavelet filtered image with detected sources (ObsID: 0403072201).

the final decision was made by a moderator upon the evaluators' comments. False detections are classified as 'point-like', 'double source', 'artefact' or 'nearby galaxy'. Among the 1514 screened candidates, 234 X-ray detections were found to originate from nearby galaxies; 245 were classified as artefacts, the majority of them being found in the X-ray emission of large, pointed galaxy clusters (Fig 5, bottom panels). An additional 'dubious' flag was assigned to sources for which the galaxy cluster nature is unclear: these mostly correspond to faint extended sources - at the C1 limit - with an overall compact emission. As of Aug. 2010, the catalogue contains 845 C1 cluster candidates, 104 being classified as dubious (App. A)

2.4 Count-rate measurements in multiple bands

The XAMIN pipeline is well suited to the count-rate measurement of moderately bright extended sources (up to a few thousands of photons). But in the case of sources occupying a large fraction of the detector or heavily contaminated by point-sources, hand-measurements are necessary in order to reach the accuracy required for an optimal application of the CR-HR method. We have thus developed a semi-interactive procedure to perform multi-band count-rate measurements and describe it below.

2.4.1 Methodology

We have developed software allowing for the masking of selected contaminating sources (mostly background or host AGNs), a careful account of the background levels and a possible redefinition of the source centre. Following paper I, we perform the measurements in the three different energy bands, well suited to the CR-HR analysis of the sample: [0.5-2], [1-2] and [0.5-1] keV. Input for the procedure are images and exposure maps for the three detectors in the given

bands. To correct for the masks, CCD gaps and detector borders, the source to be measured is assumed to be spherically symmetric, and count-rates are integrated in concentric annuli. The initial X-ray center is the centroid determined by XAMIN, but can be redefined by hand (e.g. if a CCD gap is masking part of the extended emission, and shifts the X-ray centroid). We define source count-rates as the mean number of source photons collected by the telescope during one second, corrected from vignetting (i.e. equivalent to *on-axis* measurement) and detector cosmetics (CCD gaps, etc.). Using the detector exposure maps, we derive the mean count-rate of the source in each annulus and compute uncertainties, assuming Poisson noise. A control annulus, chosen sufficiently far away from the source, but close enough to account for local variations, provides the background estimate. Following (Read & Ponman 2003), we model the background by a sum of a vignetted component (*photon* background) and an flat *particle* background, each of them being described by one parameter. The uncertainties on these parameters are derived assuming Poisson noise, and propagated to the uncertainties on the individual source count-rates.

Measurements are performed on each detector, then summed up to provide a total count-rate. A count-rate growth curve is then computed (Fig. 6), as well as a surface brightness profile. For each source, the masking areas, the source position, as well as the number and width of the annuli and the background area, are set by hand in the [0.5-2] keV energy band. These settings are then stored and used for automatically measuring count-rates growth curves in the two other bands [0.5-1] and [1-2] keV. Final measurements are always performed using the complete pointing exposure (i.e. not only the 10 ks or 20 ks data), in order to maximise the signal-to-noise ratio.

Such a procedure presents the advantage to be model-independent and does not require any spatial fitting. In turn, only aperture count-rates are available, up to a limiting radius at which the source emission vanishes in the background. For each measurement, the software provides the radius at which the integrated count-rate value shows a signal-to-noise ratio equals to 1 (i.e. compatible with background emission). The vertical dotted line displayed on Fig. 6 shows the position of this radius for a particular cluster measurement. In most cases, the integration radius set manually is very close to the automatic guess by the software, except in the few cases where the measurements in consecutive annuli are noisy (e.g. in presence of a mask or a CCD gap).

2.4.2 Assessment of the method and aperture corrections

We quantitatively evaluated the validity of our measurement procedure by means of simulated XMM observations of galaxy clusters. We used the simulation set described in Section 3 which provides a representative range of observing conditions (in terms of background and exposure time) and of galaxy cluster sizes and fluxes. Table 5 summarizes the set of simulated observations. All simulated cluster profiles are azimuthally symmetric β -models with fixed $\beta = 2/3$ (Cavaliere & Fusco-Femiano 1976). The total count-rate and core radius are taken among discrete values close to those expected in the survey. Each of the 18,000 simulated observations is processed following the steps described previously. We then applied selection criteria identi-

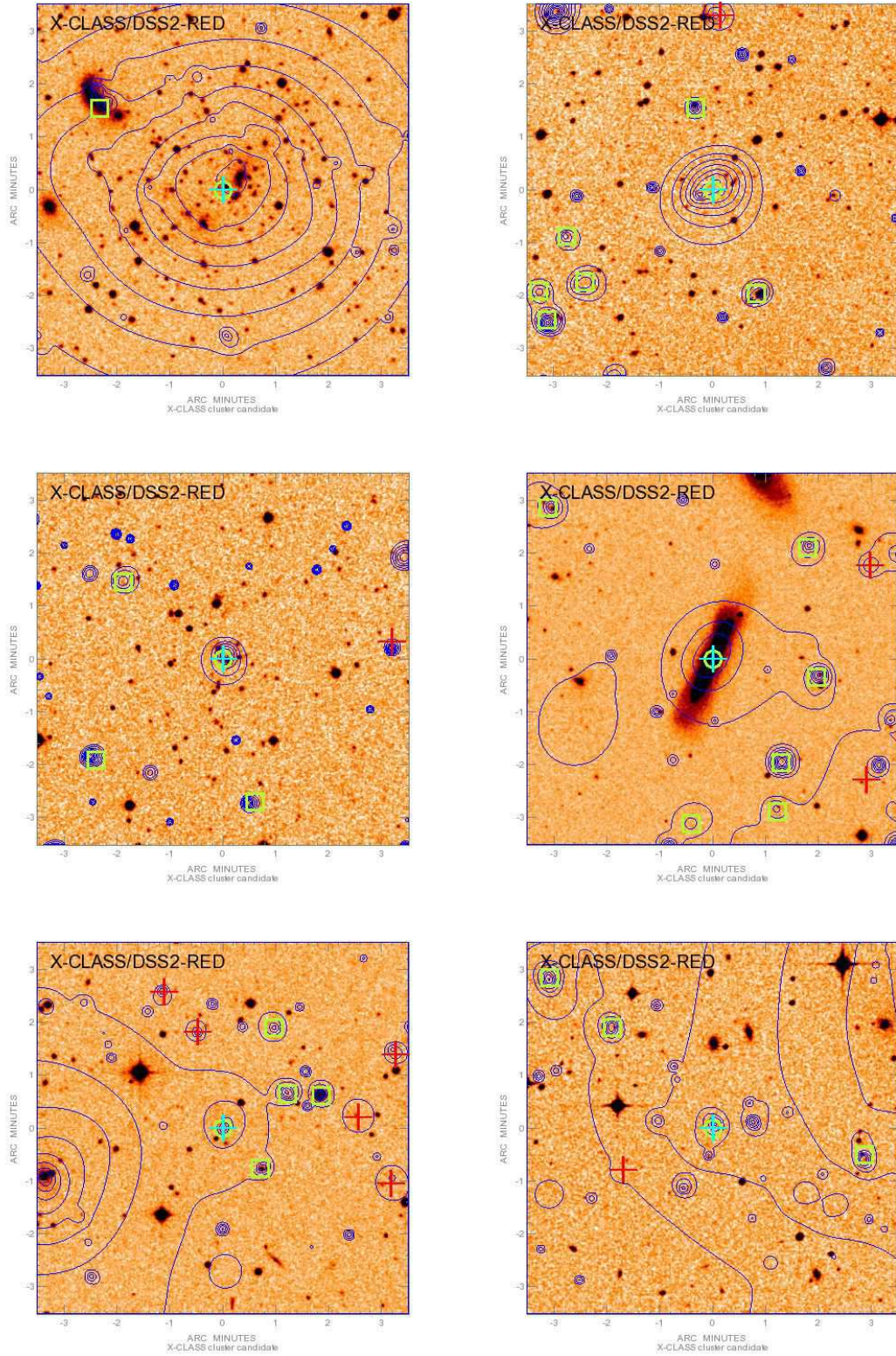


Figure 5. Illustration of the data screening classification (Sect. 2.3). From left to right, top to bottom : classification " $0 < z < 0.3$ " (known cluster A2218 $z=0.176$), " $z > 0.3$ " (indicative redshift, not used in the analysis), "Dubious", "Nearby galaxy" (NGC 4634). Both bottom panels show 'dubious' sources, likely being substructures in a close cluster or background clusters. Green circles indicate the position of C1 candidates and green boxes are others X-ray detections; the cyan cross indicates the centroid of the X-ray emission; red crosses stand for the first-pass sources that were found to have a likelihood detection smaller than 15 by XAMIN.

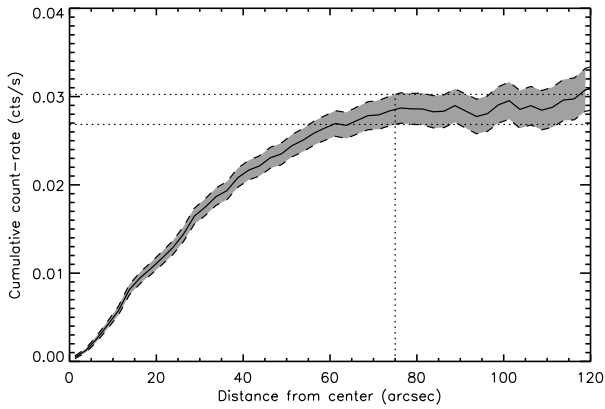


Figure 6. Example of a count-rate integration curve with associated 1σ error bars (Cluster tag 2094 in L4SDB). The vertical line indicates a S/N of one. Apparent fluctuations at large cluster-centric distances are due to uncertainties in the background subtraction.

cal to those applied for the cosmological analysis, as outlined in Sect. 4 and the count-rate of the $\sim 10,000$ selected clusters were automatically measured following the above procedure. The size of the background annulus and the boundary radius for the integration were set according to the cluster input extent.

Fig. 7 presents the results obtained for both 10 ks and 20 ks simulated pointings. Each panel shows the ratio of the measured count-rate over the true input value, as a function of measured core radii. The lack of statistics at large radii comes from the small number of extended sources detected in the simulations. The decreasing trend in this ratio as a function of input count-rate is explained by Eddington bias: at low fluxes, only clusters that pass the selection function criteria are measured. It artificially increases the mean value of the measured count-rate. Our method thus accounts for the statistical nature of the cluster sample. These results show the overall accuracy of the count-rate measurement procedure. They are in agreement with the fact that sources that are more extended are less well measured and this effect is more pronounced for higher background levels.

To correct for the flux loss due to fixed aperture measurements, we fitted in each panel a linear relation of the form $CR_{\text{mes}} = a \cdot CR_{\text{input}} + b$ (see Fig. 7). We corrected individual cluster measurements by inverting this relation, thus providing an estimate of the true count-rate in the band of interest.

2.4.3 Filter combinations and N_H values

According to the choice of the XMM guest observers, the MOS and PN observations are obstructed by one of the three EPIC filters, namely THIN1, MEDIUM and THICK. For the purpose of applying the CR-HR method, cluster count-rates must be evaluated in a unique reference filter (THIN1 in our case). We thus need to apply some a posteriori correction for using observations performed with other filters. Because filter transmission curves have different spectral dependences, these corrections are energy-dependent and we estimate them by means of empirical conversion relations:

MOS1 Filter	MOS2 Filter	PN Filter	Nbr. Point.
Thin1	Thin1	Thin1	1063
Medium	Thin1	Thin1	12
Thin1	Medium	Thin1	12
Medium	Medium	Thin1	168
Thin1	Thick	Thin1	20
Thin1	Thin1	Medium	23
Medium	Thin1	Medium	5
Medium	Medium	Medium	619
Thick	Medium	Medium	1
Medium	Thick	Medium	2
Thick	Thick	Medium	12
Thin1	Thin1	Thick	1
Medium	Medium	Thick	6
Medium	Thick	Thick	1
Thick	Thick	Thick	47
Total			1992

Table 2. Distribution of filter configurations for the set of XMM archival pointings entering the scientific analysis. Only 5% of those pointings have one or more detector observing with the Thick filter, which causes a $\sim 22\%$ dimming at 1 keV.

we form count-rate ratios obtained from a wide range of cluster spectra in the energy range of interest and fit a linear relation of the form:

$$\frac{CR(X, \text{Thin/Thin/Thin})}{CR(X, \text{Filterset})} = f\left(\frac{CR(Y, \text{Filterset})}{CR(X, \text{Filterset})}\right) \quad (1)$$

where X and Y are two different energy bands, the left-hand side representing the inverse of the filter attenuation in the considered energy band. We made use of PIMMS 4.3² and simulated XMM cluster count-rates on a grid of temperatures between 0.5 and 9 keV and at different redshifts up to $z = 1.5$. Count-rates were computed in our three reference bands ([0.5–2], [0.5–1] and [1–2] keV). We did not consider clusters too cold and too distant since they are not retained by the C1 selection function of Pacaud et al. (2006). Fifteen filter combinations out of the 27 possible ones are found in the 1992 pointings used in our analysis (Table 2), more than half of them being in the THIN1-THIN1-THIN1 configuration.

We repeated the operation for typical galactic absorption values, ranging from $N_H = 10^{20}$ to $2.10^{21} \text{ cm}^{-2}$ (see Fig. 2). Table 3 shows an example of best-fitting values for the empirical correction. The corrections are significant only if the THICK filter is used, which is consistent with the fact that the THIN1 and MEDIUM attenuations are comparable for the chosen energy bands. The relative uncertainty of these conversions was found not to exceed a few percent.

3 THE X-CLASS SURVEY SELECTION FUNCTION

This section describes the steps leading to the construction of the final cluster sample used in the cosmological analysis. We present the list of retained XMM observations and subsequently describe the image simulations leading to the cluster selection function. We finally expose the method we

² <http://heasarc.nasa.gov/Tools/w3pimms.html>

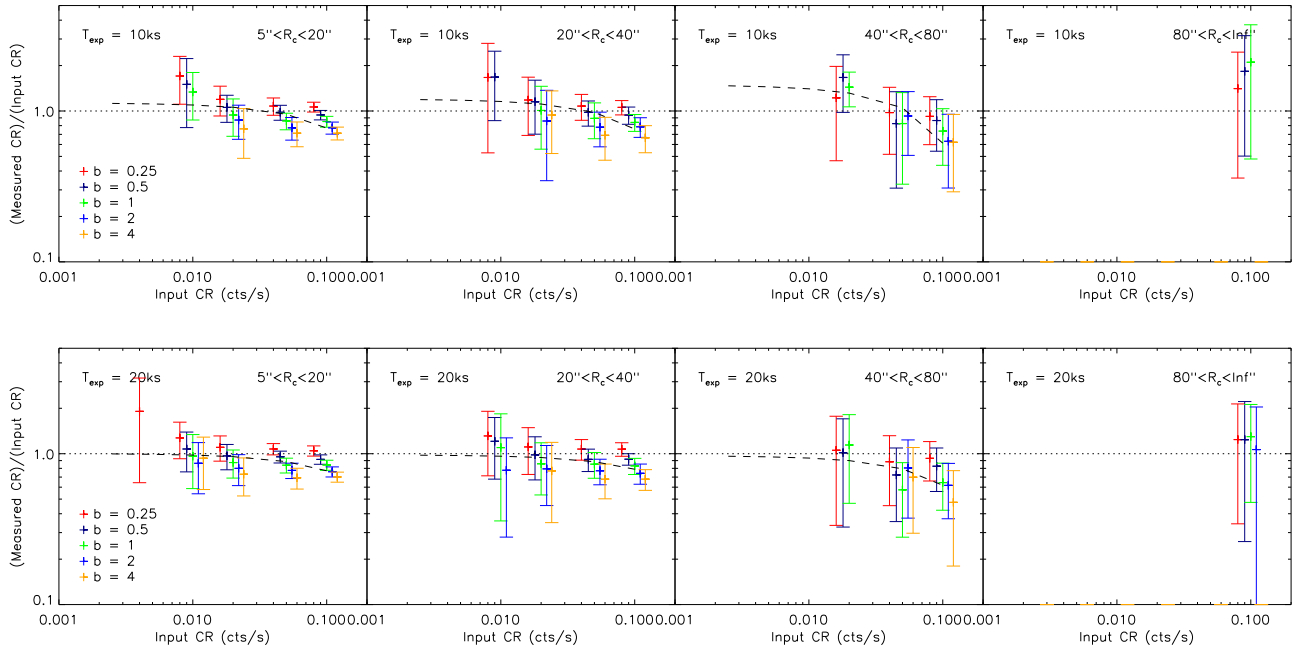


Figure 7. Aperture correction for measurements of cluster count-rates. *Top:* 10 ks simulated pointings, *Bottom:* 20 ks simulated pointings. In each panel only clusters having output core radii in the indicated range are included. Simulations were performed for various background levels as indicated by the colours. The data points have been horizontally shifted for clarity. Measured count-rates are obtained by the aperture photometry described in Sect. 2.4. Only simulated C1⁺ clusters (matching the same criteria as for the cosmological subsample) are included here. The black, dashed line shows the best linear fit used for correcting the individual count-rate measurements.

MOS1 Filter	MOS2 Filter	PN filter	C ₀	C ₁
Medium	Thin1	Thin1	1.01	0.00
Thin1	Medium	Thin1	1.01	0.00
Medium	Medium	Thin1	1.03	0.00
Thin1	Thick	Thin1	1.03	0.01
Thin1	Thin1	Medium	1.00	0.00
Medium	Thin1	Medium	1.02	0.00
Medium	Medium	Medium	1.03	0.00
Thick	Medium	Medium	1.04	0.01
Medium	Thick	Medium	1.04	0.01
Thick	Thick	Medium	1.06	0.02
Thin1	Thin1	Thick	1.10	0.09
Medium	Medium	Thick	1.14	0.09
Medium	Thick	Thick	1.15	0.10
Thick	Thick	Thick	1.17	0.12

Table 3. Example of coefficients used for the empirical filter corrections : bands $X=[0.5-2]$ keV and $Y=[0.5-1]$ keV and $N_H = 4.10^{20} \text{ cm}^{-2}$ are considered here. The correction is modeled by a linear relation of the form $x_{\text{corr}} = C_0 \cdot x_{\text{mes}} + C_1 \cdot y_{\text{mes}}$, where x_{mes} and y_{mes} are count-rates measured with the same particular set of filters, respectively in bands X and Y and x_{corr} , the corrected count-rate as it would be measured in band X with the highest transmission set of filters (THIN1-THIN1-THIN1). These conversions were found to be accurate at the few percent level for clusters with temperatures ranging from 0.5 to 9 keV and redshifts out to 1.5, as long as their location in the temperature-redshift plane is covered by the C1 selection (see text).

have developed for evaluating the statistical bias due to the presence of numerous pointed clusters in the XMM archive.

3.1 The cosmological subsample

The cluster sample described in Sect. 2 contains 845 C1 sources detected in a homogeneous way in the XMM archival data. In order to perform the cosmological analysis by means of the CR-HR method, we extracted a high signal-to-noise ratio subsample as follows.

We first selected a more homogeneous data set, i.e. by excluding pointings (1) with a high background, (2) with one or more detectors not being in full-frame mode and (3) those centered on very nearby, luminous clusters (see examples on Fig. 8). For this purpose, we inspected the 2409 pointings by eye. In the end, the surveyed area used for the cosmological fits consists of 1992 pointings (Table 1)

We defined a sub-class of galaxy clusters called C1⁺ by selecting all sources having an Extent Likelihood above 40 and an extent greater than 5 arcsec. Only C1⁺ sources within 10 arcmin off-axis of their parent pointing and not flagged as dubious were considered. Defining CR as the [0.5-2] keV measured count-rate and HR as the ratio between the [1-2] keV and [0.5-1] keV count-rates, we imposed clusters to have $0.009 < CR < 0.5 \text{ cts/s}$ and $0.05 < HR < 2$. Finally, the cosmological subsample consists of 347 clusters.

3.2 Description of the simulations

3.2.1 Principle

We use an updated version of INSTSIMULATION (Valtchanov, Pierre, & Gastaud 2001; Pacaud et al. 2006) to generate fake XMM observations, taking into account the main characteristics of the XMM EPIC instruments.

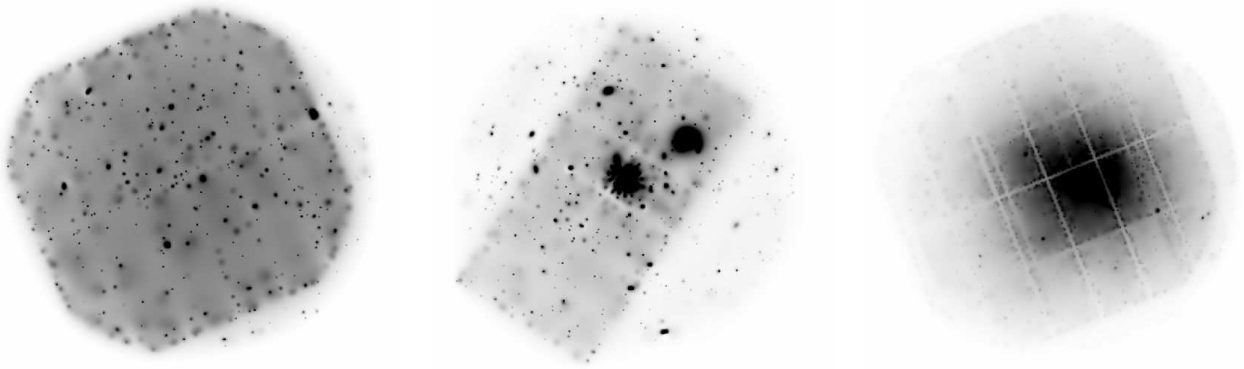


Figure 8. Three examples of pointings excluded from the cosmological analysis (images have been filtered by wavelets). *Left panel:* this pointing shows a high background on the PN detector which has not been optimally filtered by the pre filtering procedure due to long continuous periods of background flares (ObsId: 0039140101). *Central panel:* the PN detector was working in Large Window mode thus not collecting photons from the entire field of view (ObsId: 0083150401). *Right panel:* observation of Coma extending over a large part of the field of view thus preventing the detection of background sources (ObsId: 0300530301).

Table 4. Number of detected clusters in the X-CLASS database. Clusters entering the cosmological analysis are C1⁺ sources not classified as ‘dubious’, within 10 arcmin off-axis and having $0.009 < CR < 0.5$ cts/s (count-rate in [0.5-2] keV) and $0.05 < HR < 2$ (ratio [1-2] keV / [0.5-1] keV).

C1 sources detected in the 2409 X-CLASS pointings	845
C1 ⁺ sources :	745
- classified as ‘dubious’,	74
- within 10 arcmin off-axis,	630
- entering the cosmological analysis	347

In particular, an analytic vignetting model and a detector mask are superimposed to the simulated sources, as well as instrumental and photon backgrounds. The shape and off-axis dependency of the PSF is modeled by using the MEDIUM model from the XMM calibration files. Apart from the peculiar observations of bright, saturated sources, or extremely extended sources, the simulation set captures the most important features impacting the detection and the characterization of the sources. We performed two sets of simulations: one with point-like sources only, and the other with clusters and point-like sources.

3.2.2 Point-like sources only

The first set of simulations without extended sources serves as a test for contamination and for parametrizing the background level on the instruments. Point-like sources are distributed across the field of view, following a sampled $\log N - \log S$ taken from (Moretti et al. 2003) in the [0.5-2 keV] band. Conversion from flux to count-rate is performed assuming a constant MOS to PN count-rate ratio, regardless of the source spectral distribution. The flux lower bound is chosen accordingly to the exposure time so as to give ~ 2 photons on-axis (i.e. below the XMM detection limit). Non-resolved AGN photon background is added following values from (Read & Ponman 2003), then corrected from the estimated fraction of AGNs resolved by the pipeline. This background component is vignettted, thus showing a strong

off-axis dependence. We finally add the non-vignettted particle background component using the standard values from Read & Ponman (2003) multiplied by an arbitrary factor $b = 0.25, 0.5, 1, 2$ or 4 so as to investigate the impact of pointing-to-pointing background variations on the detection efficiency. For each background value, 540 pointings are simulated both at 10 and 20 ks exposure times.

Each of these pointings is processed by the XAMIN pipeline described in Sect. 2, exactly in the same way as real observations. In particular, an extended model fit is performed over each detected point-source to evaluate the contamination of the cluster sample.

3.2.3 Extended source simulations

Similar simulations are performed by adding clusters assumed to be spherically symmetric sources and defined by a $\beta = 2/3$ profile; apparent core radii r_c range from 10 to 100 arcsec and total count-rates from $2.5 \cdot 10^{-3}$ to 0.1 cts/s. From 4 to 8 simulated clusters are injected in each pointing, depending on their angular size, and we avoided source overlap by defining exclusion sectors in the XMM field of view. In total, some 87000 extended sources were simulated over more than 18000 pointings (Table 5). In order to reproduce the effects of point source contamination, a population of point-like sources was added as described in the previous section.

Each pointing is processed by the pipeline and positions of the input extended sources are correlated with the output positions within a 37 arcsec radius. In case of multiple matches, the detected source with the highest Extent Likelihood is chosen as the best matching counterpart and all others are discarded. Fig. 9 (top panel) shows three examples of simulated pointings in different observing conditions, along with the corresponding pipeline results.

Table 5. Summary of the extended-source simulations in XMM images. Last column indicates the number of simulated clusters out to an off-axis of 10 arcmin. Simulations were performed for exposure times of 10 and 20 ks and five background levels ($b=0.25, 0.5, 1, 2$ and 4). The total number of simulated and processed pointings is 18140 and the total number of clusters amounts to ~ 87000 .

Input count-rate (10^{-2} cts/s)	Input core radius					Total
	10"	20"	50"	100"		
0.25	450	450	750	240	–	1890
0.5	450	450	750	240	–	1890
1.0	450	450	750	240	–	1890
2.0	450	450	750	240	–	1890
5.0	100	100	150	240	–	590
10.0	100	100	150	240	–	590

3.3 Analysis of the simulations - selection criteria

3.3.1 Contamination by spurious and point-like sources

Following Pacaud et al. (2006) we report for each detected source its location in a two-parameter space Extent/Extent-Likelihood, as shown in Fig. 9, middle panels. In this figure, green symbols represent point-like sources, magenta symbols are for extended sources and red points stand for spurious detections, i.e. detections in the point-only simulations which are not associated to input sources within the 6" correlation radius. Fig. 9 shows the good stability of the C1⁺ criterion across the range of exposure times and background levels, in terms of contamination by point-like sources and spurious detections. From our simulations, we expect the number of contaminating sources (i.e. point-sources interpreted as extended sources) not to exceed one in every 300 pointings for normal observing conditions (10 ks, low background).

3.3.2 Efficiency of the extended sources detection

We then derive the C1⁺ detection efficiency by taking all sources in the 0–10 arcmin off-axis range. Bottom panels of Fig. 9 display the probability of detecting a C1⁺ cluster as a function of its total input count-rate and its input core radius, as derived from our simulations. From these results, it clearly appears that the selection is not flux-limited, but rather surface-brightness limited. These curves also reveal the expected increase in efficiency from 10 to 20 ks and for lower background levels. The sharp decrease observed in the 20 ks selection for high count-rates (~ 0.06 – 0.1 cts/s) and small core radii (< 20 arcsec) indicates that these sources are identified as point-like sources by the pipeline; such objects, however, are unlikely to appear in real observations. We derived similar probability functions for the ten simulated configurations (10 and 20 ks exposures and five background levels).

Then, for any given pointing in the survey, we estimate its background parameter (b). To this purpose, we measure local background estimates at several locations on the detectors and compare them to the values found in the simulated observations for which b is known. We finally derive the selection function of each XMM observation entering the cosmological analysis.

3.4 The survey geometrical area

For the cosmological analysis, we consider only sources within a 10 arcmin radius around each pointing center, thus removing regions of the detectors where the point spread function has an elongated shape and the vignetting factor is greater than 50%. Because of the multiple overlaps between pointings, we estimate the net area by means of a Monte-Carlo integration. If two or more pointings of the same exposure time overlap, the intersecting area is equally distributed between those pointings. If one 20 ks pointing and one 10 ks pointing overlap, the intersecting area is fully attributed to the deeper pointing. This set of rules is thus compatible with the procedure applied for removing duplicate detections in the catalogue (Sect. 2). The net total area covered by the 1992 pointings is 90.3 deg^2 .

3.5 Correcting for the target bias in the XMM archive

In all cluster serendipitous surveys to date, it has always been implicitly assumed that discarding the central target of the considered pointings (along with subtracting the corresponding survey area) would not statistically affect the studied cluster population. It is not the purpose of the present paper to verify these past assumptions, but in the case of serendipitous surveys based on the XMM archive, this hypothesis is questionable. Among the 7716 archival observations available by May 2010, 1008 of them pertain to pointed observations of galaxy clusters. Out of the 347 clusters selected for the present cosmological analysis, 92 of them are central targets (within 3 arcmin offaxis). One cannot simply discard them or include them (or ignore the complete pointing) in the statistical analysis, because the process of target selection from guest observers is highly subjective as well as motivated by practical constraints. This is particularly true for distant clusters, as only the brightest ones could be observed.

In this section, we describe the method that we have developed to account for the target selection bias and correct for its impact in the cosmological analysis. This bias is hard to model from first principles as it depends on the history of the XMM observing programs. Basically, we make use of the fact that pointed galaxy clusters are preferentially located at the center of the XMM field of view and split our sample in two subsamples to apply a joint correction.

3.5.1 Off-axis source distribution

Fig. 10 shows the distribution of detected clusters as a function of off-axis distance. The excess of sources in the 0–5 arcmin range is conspicuous, as well as the stabilization at higher radii. There is a factor of 2 between the density of sources in the ‘outer’ regions of the detectors and the ‘inner’ regions. Part of this difference stems from the better sensitivity in the central part of the XMM FoV but a also from a number of pointed clusters. We label by ‘in’ and ‘out’ the corresponding two subsamples and make the hypothesis that all pointed clusters are found in the ‘in’ sample.

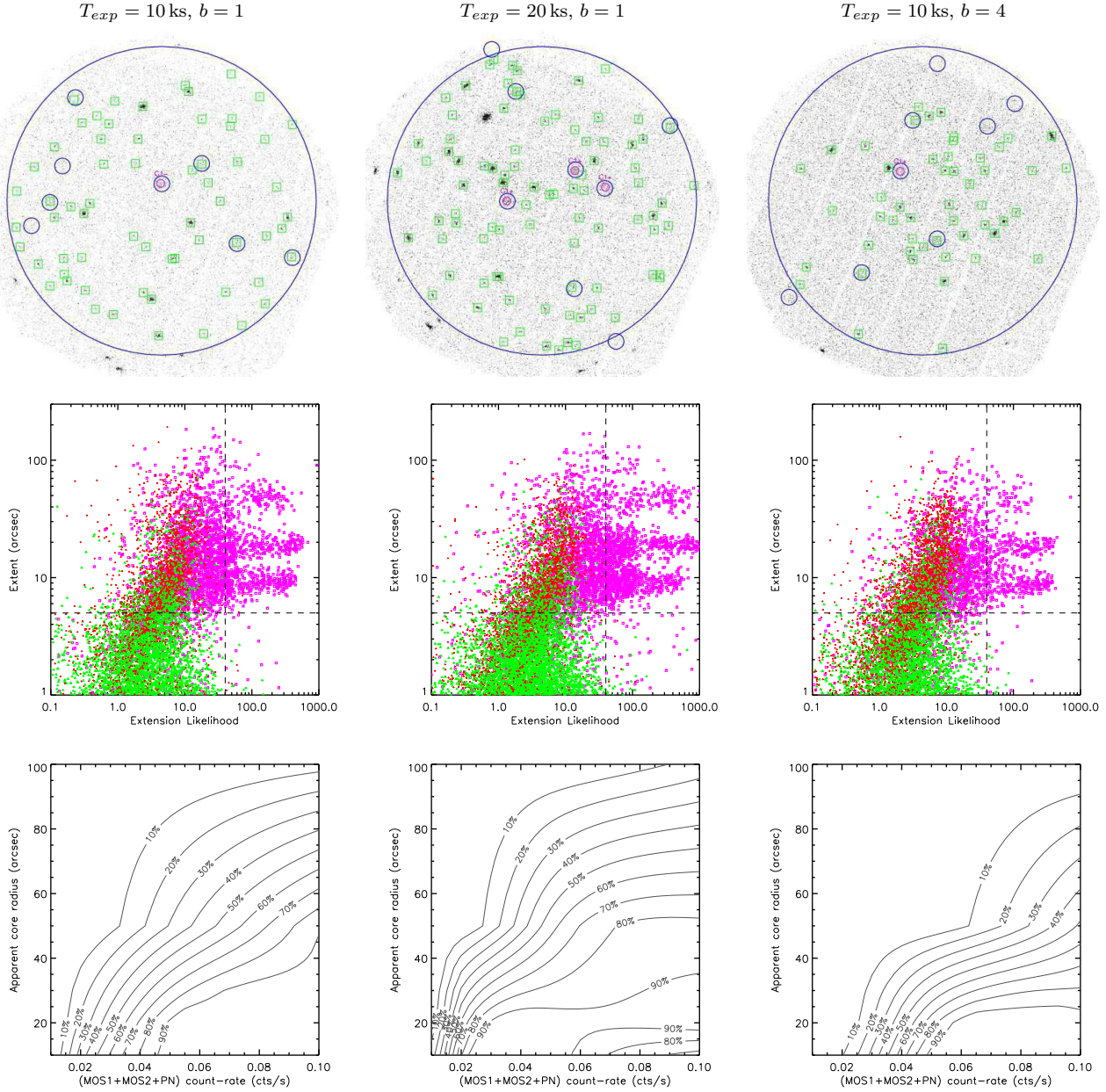


Figure 9. The X-CLASS selection function. We present the results of simulations performed for three pointing configurations (different exposure times and background levels) among the 10 simulated configurations. *Top:* Example of simulated XMM observations. Blue circles show the locations of simulated 20 arcsec core-radius clusters and magenta circles denote detections classified as C1⁺ by the pipeline. Green boxes are for the remaining, unclassified sources (including point sources). The radius of the large blue circle is 13 arcmin. *Middle:* Distribution of detected sources in the Extent-Likelihood/Extent plane. Recovered clusters are in magenta, point-like sources in green and spurious detections in red. Vertical and horizontal lines delimit the C1⁺ classification (EXT_ML > 40 and EXT > 5); the discreteness of the Extent distribution reflects the input core radius values (Table 5) *Bottom:* Corresponding detection probability for the C1⁺ sources as a function of the input [0.5-2] keV count-rate and the input core-radius. [2.5.10⁻³, 5.10⁻³, 0.01, 0.02, 0.05, 0.1]

3.5.2 Bias model

We display in upper panel of Fig. 11 the count-rate distribution of sources in both subsamples per unit sky area. According to Fig. 10, there is a factor ~ 2 between both distributions, but the excess is not uniformly spread over the range of count-rates. For instance the factor 3 excess around CR ~ 0.15 cts/s corresponds to clusters with fluxes $\sim 1 - 2.10^{-13}$ ergs/cm²/s typical of those found in *ROSAT* serendipitous surveys: 160d (Vikhlinin et al.

1998b), 400d (Burenin et al. 2007), WARPS (Jones et al. 1998) and SHARC (Adami et al. 2000; Romer et al. 2000) – see Piffaretti et al. (2011) for a thorough compilation of *ROSAT* cluster catalogues. Clusters from the *ROSAT* All-Sky Survey are more than ten times brighter on average and are thus excluded from our cosmological sample (limited to CR < 0.5 cts/s).

Because of the finite number of clusters of given flux across the entire sky, the sample dubbed ‘out’ does not ex-

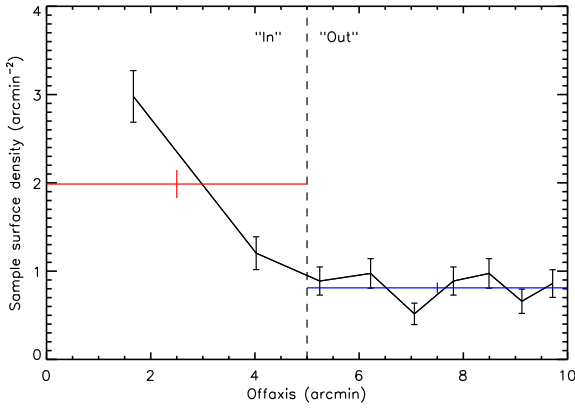


Figure 10. Surface density of clusters as a function of off-axis distance, for the selected subsample used in the cosmological analysis (black curve). The red and blue points are the average surface densities in the inner [0-5] arcmin and the outer [5-10] arcmin regions respectively. The factor ~ 2 between the two values is mainly caused by the presence of pointed clusters in the archival data.

actly reflect the cluster population as it lacks all clusters being pointed. As both subsamples derive from the same parent distribution, we use a single parameter for the inner excess and the outer dearth of clusters. We detail in App. B our procedure to infer its value, taking into account the effective areas of both the inner and outer part of the XMM field of views. All count-rate bins j are treated separately and we compute a bias factor F_j (Fig. 12) whose value represents the ratio between the observed number of clusters in the considered bin and the actual expected number of clusters if no object were pointed. By definition, F_j is always greater or equal to one.

4 THE COSMOLOGICAL ANALYSIS

This section presents the analysis performed with the subsample of 347 C1⁺ clusters selected over our effective area of 90 deg² from the XMM archival data. We first show the resulting CR–HR diagram, which is the sole observable quantity used in the cosmological analysis. We then describe its modeling from first principles, taking into account a cosmological model, X-ray cluster scaling-laws and the various selection effects affecting the sample. We finally show the results obtained by a Monte-Carlo Markov Chain sampling.

4.1 Sample CR–HR distribution

Following Sect. 2, count-rates for all 347 clusters entering the analysis have been measured in three energy bands: [0.5–2], [0.5–1] and [1–2] keV. These values have been corrected from flux loss due to the finite aperture measurement and, if necessary, converted in the THIN1 filter set. We compute the hardness ratio of each cluster by dividing the [1–2] keV count-rate by the [0.5–1] keV measurement and report its value in a CR–HR plane, where CR stands for the wide band measurement. Fig. 13 shows the distribution of clusters in this diagram, along with associated error bars. The

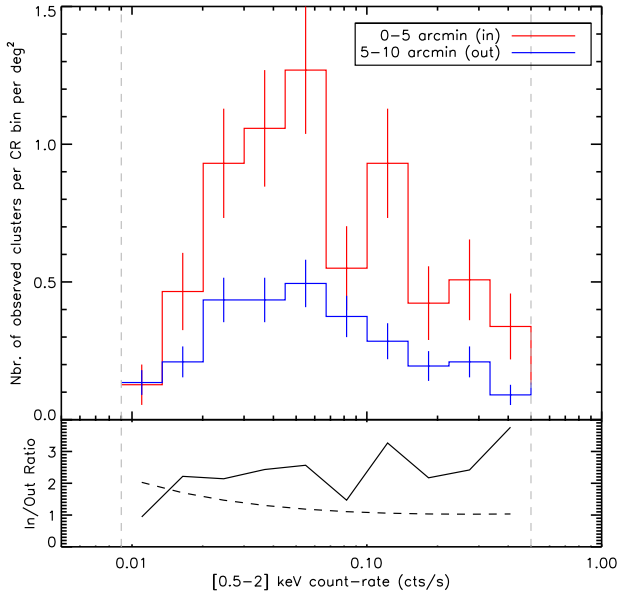


Figure 11. *Top panel:* count-rate distribution of the sources found within 5 arcmin off-axis (red) and between 5 and 10 arcmin off-axis (blue) for the cosmological subsample containing 347 clusters (all count-rates are rescaled to their on-axis values). *Bottom panel:* the plain curve shows the ratio between the two histograms shown in the top panel. The dashed line is the ratio that one would expect from the sensitivity gradient only.

distribution is spread over the range of count-rates peaking around 0.3–0.4 cts/s.

4.2 Modelling the CR–HR distribution of sources

We describe the main steps of the computation of the CR–HR distribution of clusters, starting from the halo mass function and using the survey selection function. These steps are more thoroughly detailed in paper I.

4.2.1 Halo mass and redshift distribution

We assume a Λ CDM cosmological model and a flat Universe ($\Omega_m + \Omega_\Lambda = 1$) with no-evolving dark energy ($w = -1$). Starting from the primordial, scale-invariant power spectrum with slope $n_s = 0.961$ (Dunkley et al. 2009) we make use of the Eisenstein & Hu (1998) fitting formula for the transfer function to obtain the linear power-spectrum. We use the Tinker et al. (2008) fit to the mass function and obtain the comoving density of haloes per mass interval dM_{200b} about M_{200b} at redshift z , where M_{200b} is the mass within a radius R_{200b} inside which the mean density is 200 times the mean density of the Universe at that redshift. We convert this distribution into the sky-projected density of clusters per redshift slice. Only Ω_m and σ_8 (normalization of the power spectrum at a scale $R = 8h^{-1}$ Mpc) are let free in the analysis. All other parameters are held at their WMAP-5 value (Dunkley et al. 2009), in particular $H_0 = 72.4$ km/s/Mpc.

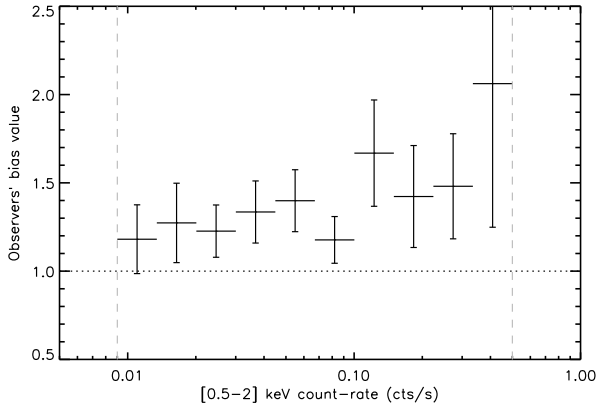


Figure 12. Bias factor F_j for cluster counts (see App B) due to the presence of pointed clusters in XMM archival data. F_j is computed in 10 count-rate bins and evaluated by comparing the density of clusters in the inner [0-5] arcmin to the [5-10] arcmin density, taking into account the higher sensitivity around the EPIC optical center. The bias value is the ratio between the observed number of sources in a given bin and the number expected for a sample without pointed clusters. We use it as an empirical correction for the final sample of 347 clusters selected for the cosmological analysis.

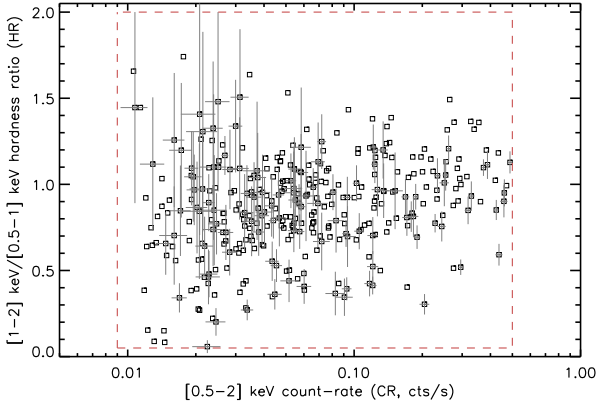


Figure 13. CR-HR diagramme for the 347 clusters pertaining to the cosmological subsample. Not all error bars are displayed in order to ease visualization. The dashed box delimitates the region used for the cosmological fit.

4.2.2 Cluster emissivity and extent

We assign to each cluster three quantities describing its X-ray emission: its redshift z , its plasma temperature T (X-ray spectral temperature) and its bolometric luminosity L_X integrated over its complete extent. We consider a mean metallicity of $0.3 Z_\odot$. The conversion from cluster mass to temperature and luminosity is achieved thanks to scaling relations of the form:

$$\frac{M_{200c}}{10^{14} h^{-1} M_\odot} = 10^{C_{MT}} \left(\frac{T}{4 \text{ keV}} \right)^{\alpha_{MT}} E(z)^{-1} (1+z)^{\gamma_{z,MT}} \quad (2)$$

$$\frac{L_X}{10^{44} \text{ ergs/s/cm}^2} = 10^{C_{LT}} \left(\frac{T}{4 \text{ keV}} \right)^{\alpha_{LT}} E(z) (1+z)^{\gamma_{z,LT}} \quad (3)$$

To account for the intrinsic scatter in those relations, we assume two parameters $\sigma_{lnT|M}$ and $\sigma_{lnL|T}$ constant over the entire redshift, mass and temperature ranges considered in our analysis. Throughout this work we will use the M_{200c} - T relation from Arnaud, Pointecouteau, & Pratt (2005) derived for their hot cluster sample (see Table 6).

As discussed in paper I, a reasonable choice for the emissivity profile of clusters is a β -model (Cavaliere & Fusco-Femiano 1976) with $\beta = 2/3$ and a core radius r_c scaling with R_{500c} , parametrized by $x_{c,0} = r_c/R_{500c}$ at all redshifts and masses. This parameter is critical as it enters in the selection function describing the observed population of clusters.

4.2.3 Instrumental model and measurement errors

The next steps consist in converting z , T and L_X into observable quantities and fold the cluster distribution into the selection function in order to obtain a CR-HR diagram for a given set of model parameters. Ideally, one should compute this distribution separately on each pointing and sum up their independent contributions to derive the complete CR-HR diagram. In order to avoid excessively large computational times we decided to group pointings by similar N_H and background values.

We use APEC spectral models with a metallicity of $0.3 Z_\odot$ along with EPIC XMM response matrices to obtain count-rates in the three bands of interest. They represent the expected number of source events per second impacting the telescope cameras mounted with THIN1 filters. The [0.5-2] keV count-rate as well as the cluster apparent core-radii are then derived. Finally, the sample selection function is used to compute the expected distribution of clusters. Measurement errors are included by convolving the CR-HR distribution with an error model using the statistical uncertainties from the count-rate measurements.

To fully model the cluster population we add a supplementary step to the methodology presented in paper I: the CR-HR model distribution is multiplied by the bias value $F(CR)$ as computed in Sect. 3 (see Fig. 12) to account for the excess of sources due to pointed observations.

4.3 Likelihood and MCMC sampling method

Given a set of parameters, the expression for the likelihood \mathcal{L} is expressed following e.g. Cash (1979) by dividing the CR-HR two-dimensional space in narrow bins such that each bin contains at most one cluster. Assuming Poisson statistics in each bin, we can write:

$$\ln \mathcal{L} = \sum_i \ln \left(\frac{dn}{dCR dHR} (CR_i, HR_i) \right) - \int_{CR_{\min}}^{CR_{\max}} \int_{HR_{\min}}^{HR_{\max}} \frac{dn}{dCR dHR} dCR dHR \quad (4)$$

where we have neglected the constant term including the size of the bins as we will consider likelihood ratios only. In the equation above, the sum runs over the 347 selected clusters. The integral is computed for $0.09 \leq CR \leq 0.5$ and $0.05 \leq HR \leq 2$ and simply represents the expected number of clusters within this CR-HR region. The modeled number density contains the effect of measurement errors

and pointed cluster bias and includes the selection function and its variations over the surveyed area, thus is as close as possible to the real CR–HR distribution of sources. We summarize in Table 6 the choice of parameters and priors we made for the different cases studied.

Confidence intervals and mean values for the parameters being studied are obtained via the Bayesian formalism and are computed from the posterior distribution of parameters given the CR–HR diagram and the underlying model. In this study, we limit ourselves to a maximum of 5 free parameters, for which a Monte-Carlo Markov Chain (MCMC) likelihood exploration becomes competitive with a grid-based computation. We use a custom Metropolis-Hastings sampler that produces MCMC chains. After a so-called *burn-in* period, the chain reaches a stationary state representative of the actual posterior parameters distribution. The ‘jump’ function is taken as a multivariate gaussian distribution with covariance matrix $C_{\mu\nu}$ computed with (see paper I for a more thorough description and references therein):

$$F_{\mu\nu} = C_{\mu\nu}^{-1} = \sum_i \frac{1}{\mathcal{O}_i} \frac{\partial \mathcal{O}_i}{\partial \theta_\mu} \frac{\partial \mathcal{O}_i}{\partial \theta_\nu} \quad (5)$$

where \mathcal{O}_i stands for the binned density $dn/dCR/dHR$ and θ is the set of varying parameters. The PDF ‘jump’ function from the current parameter set θ_n to the new one θ thus writes :

$$p(\theta|\theta_n) \propto \exp\left[-\frac{1}{2} {}^T(\theta - \theta_n) F_{\mu\nu} (\theta - \theta_n)\right] \quad (6)$$

For each chain we extract the mean value of the sampled parameters and compute the associated highest density intervals. Such an interval contains $(1 - \alpha)100\%$ of the posterior probability and ensures that the posterior density within the interval is always greater than outside. We choose $\alpha = 0.32$ which, in the case of a normal distribution, corresponds to the $1-\sigma$ boundaries of the distribution. The MCMC analysis is performed using the R-package BOA (Smith 2007). Unless otherwise stated, best-fit results are quoted using the mean of the posterior distributions (and not the maximum likelihood estimate).

5 RESULTS

Our methodology, as presented in paper I, assumes that local scaling laws are known, we thus focus on their evolution and on the cosmological parameter determination. Different expressions for the local scaling laws are found in the current literature. This is particularly true for the L–T relation (e.g. Arnaud & Evrard 1999; Branchesi et al. 2007; Maughan et al. 2012), likely because of the different populations being taken into account (Pratt et al. 2009; Mittal et al. 2011), but also because of different selection effects. However, our cluster sample is not quite large enough to allow for a simultaneous fit of the local scaling laws, of their evolution and of cosmology. We thus proceed with a step by step approach to select a local L–T that matches well our sample, focusing on two relations from Pratt et al. (2009). We use these relations since they are well suited to the mass range of our sample, contrary to, e.g. Mantz et al. (2010b) scaling relations which have been derived for much more massive clusters. We first set the cosmology to the

WMAP-5 values and select a ‘best’ relation by comparison to our data and to published $\log N$ – $\log S$ from the literature. We then release cosmological parameters to perform an enlarged fit of our data and finally show that the selected L–T still adequately describes our clusters. In all cases, we always assume a flat Λ CDM Universe.

5.1 Fixed cosmology, fixed local scaling laws

5.1.1 Constraints from the CR–HR distribution

We first fit $\gamma_{z,MT}$ and $\gamma_{z,LT}$, the parameters governing the non-self-similar behaviour of the M–T and L–T relations, as well as $x_{c,0}$, the cluster size. Other parameters are set according to Table 6, in particular Ω_m and σ_8 which are held at their WMAP-5 value and we assume that scaling relations are perfectly known. For the temperature to luminosity conversion we consider the numerical values of Pratt et al. (2009) using two of their $L_1 - T_1$ relation without core excision. One of them has been computed for all clusters present in their sample (‘ALL’) while the other (‘NCC’) excludes all clusters showing high central gas density and thus hosting a cool core. As the intrinsic scatter in these relations depends on the population of clusters in the sample, we use two test values, $\sigma_{lnL|T} = 0.3$ and 0.7 ; these values correspond to the lowest and the highest scatter found in Pratt et al. (2009). We emphasise here that we allow us to somewhat generalise their results since, formally, scatter values of 0.3 and 0.7 are associated to the ‘NCC’ and ‘ALL’ samples respectively.

The fit results with associated uncertainties are quoted in Table 7, along with an indication of the relative likelihood for each test case. The Cash statistics $C = -2\ln \mathcal{L}$ is evaluated at the mean of the posterior distribution. As changing from one L–T relation to the other involves 3 parameters in our model (α_{LT} , C_{LT} , $\gamma_{z,LT}$), the difference between C and the (unknown) minimal value C_{min} obtained when all 6 parameters are let free behaves as a χ^2 with 3 degrees of freedom (Cash 1979). This allows us to put a lower boundary to the χ^2 of all four fits, e.g.:

$$\begin{aligned} \chi_{ALL,0.7}^2 &= C_{ALL,0.7} - C_{min} \\ &> C_{ALL,0.7} - C_{NCC,0.7} = 8.4 \end{aligned}$$

Because the probability for χ_3^2 to be greater than 8 is $\sim 5\%$, it indicates that our data prefers the ‘NCC’ scaling relation with a large intrinsic scatter to the three other scaling laws.

5.1.2 Comparison with published $\log N$ – $\log S$ distributions

We cross-check the outcome of our 3-parameter fit by comparing the resulting cluster $\log N$ – $\log S$ to that from other surveys. We show on Figure 14 the $\log N$ – $\log S$ computed with two local L–T (‘NCC’ and ‘ALL’, $\sigma_{lnL|T} = 0.7$). We display the result with and without the $(1+z)^{\gamma}$ evolution factor in the scaling laws. In the former case, we used our best-fit parameters $\gamma_{z,MT}$ and $\gamma_{z,LT}$ from Table 7. We note that the value of $x_{c,0}$ has no impact on the predicted $\log N$ – $\log S$ since such a distribution is meant to be flux limited. The REFLEX data correspond to Böhringer et al. (2001) best-fit power-law converted into a $[0.5-2]$ keV $\log N$ – $\log S$ using a constant factor calculated for a APEC plasma at $z = 0$ with $T = 5$ keV. RDCS values are from Rosati et al. (1998) and

Table 6. List of parameters used in this work. The cosmological parameters are from WMAP-5 (Dunkley et al. 2009). Numbers in brackets indicate the uniform priors applied in the MCMC fitting procedure. When fixed, Ω_m and σ_8 are held at their WMAP-5 values, namely $\Omega_m = 0.249$ and $\sigma_8 = 0.787$. ‘ALL’ and ‘NCC’ refer to the corresponding L–T relations from Pratt et al. (2009).

Parameter	Fixed value or [prior range]	Description
Ω_m	[0.09 – 1]	(Flat Universe)
Ω_Λ	$1 - \Omega_m$	
Ω_b	0.043	
σ_8	[0.05 – 2]	
n_s	0.961	
h	0.72	
α_{MT}	1.49	$M - T$ power-law index
C_{MT}	0.46	$M - T$ logarithmic normalization
$\gamma_{z,MT}$	[−4, 4]	$M - T$ evolution index
$\sigma_{lnT M}$	0.1	$M - T$ constant logarithmic dispersion
α_{LT}	‘ALL’: 2.7, ‘NCC’: 2.9	$L - T$ power-law index
C_{LT}	‘ALL’: 0.52, ‘NCC’: 0.40	$L - T$ logarithmic normalization
$\gamma_{z,LT}$	[−5, 3]	$L - T$ evolution index
$\sigma_{lnL T}$	0.3 or 0.7	$L - T$ constant logarithmic dispersion
$x_{c,0}$	[0 – 0.9]	β -model core radius scaling wrt. R_{500c}

Table 7. Best-fit values for the evolutionary parameters $\gamma_{z,MT}$, $\gamma_{z,LT}$ and the geometrical scaling factor $x_{c,0}$ for a fixed cosmology. Quoted results are the mean and 68% confidence intervals obtained by fitting the X–CLASS CR–HR distribution, while cosmological parameters are held fixed at their WMAP-5 value and only those 3 parameters are varied. The $C = -2 \ln \mathcal{L}_{max}$ values are computed at the location of the best-fit parameters and differences are quoted relative to that obtained for ‘NCC’ with large scatter (2nd column). ‘ALL’ and ‘NCC’ refer to the corresponding L–T relations from Pratt et al. (2009)

Local L–T:	NCC		ALL	
$\sigma_{lnL T}$:	0.3	0.7	0.3	0.7
$\gamma_{z,MT}$	0.60 ± 0.15	0.32 ± 0.13	0.17 ± 0.18	$-0.13^{+0.16}_{-0.12}$
$\gamma_{z,LT}$	-1.23 ± 0.41	$-1.30^{+0.54}_{-0.37}$	$-2.25^{+0.61}_{-0.48}$	$-2.06^{+0.56}_{-0.43}$
$x_{c,0}$	0.17 ± 0.02	0.26 ± 0.03	0.27 ± 0.02	0.39 ± 0.04
$C - C_{NCC,0.7}$	7.9	(0)	9.1	8.4

160d and 400d correspond respectively to Vikhlinin et al. (1998b) and Burenin et al. (2007).

From this figure it turns out that the ‘ALL’ relation predicts too many clusters compared to observations from other authors, particularly for the brightest, most massive, nearby clusters. Conversely, the ‘NCC’ scaling relation (also assuming $\sigma_{lnL|T} = 0.7$) is less discordant and our proposed evolution nicely fits the low-flux $\log N$ – $\log S$ from the RDCS and the 400d surveys.

5.2 Free Ω_m and σ_8 , fixed local scaling law

We now relax Ω_m and σ_8 while fitting the CR–HR diagram, in addition to $\gamma_{z,MT}$, $\gamma_{z,LT}$ and $x_{c,0}$, thus allowing 5 parameters to vary in total. We consider the ‘NCC’ relation with $\sigma_{lnL|T} = 0.7$ as our reference L–T relation and keep it fixed in the analysis. Figure 15 shows the resulting posterior distribution obtained from the MCMC chains. The mean value

and associated 1- σ error bars for each parameter are :

$$\begin{aligned}
 \Omega_m &= 0.24^{+0.04}_{-0.09}, \\
 \sigma_8 &= 0.88^{+0.10}_{-0.13}, \\
 \gamma_{z,MT} &= 0.83^{+0.45}_{-0.56}, \\
 \gamma_{z,LT} &= -1.3^{+1.3}_{-0.7}, \\
 x_{c,0} &= 0.24 \pm 0.04.
 \end{aligned}$$

We note that the values for the three last parameters are consistent with the previous results from the 3-parameter fit. Figure 16 illustrates the good agreement between the observed CR–HR distribution and the best-fit model. Using the best-fit model we predict a total amount of 369 clusters in the region where the fit is performed (red dashed box on Fig 16) which is comparable to the 347 clusters actually present in the analysis. We note the presence of a few outliers that will be discussed in the next section.

We show on Figure 17 the cluster $\log N$ – $\log S$ predicted by this set of best-fit parameters, along with the 1- σ lower- and upper-boundaries obtained by propagating the posterior covariance matrix from the MCMC analysis. The $\log N$ – $\log S$ agrees well with the reference $\log N$ – $\log S$ curves, especially in the range $10^{-14} - 2.10^{-13}$ ergs/s/cm². This interval roughly corresponds to the count-rate region probed by our CR–

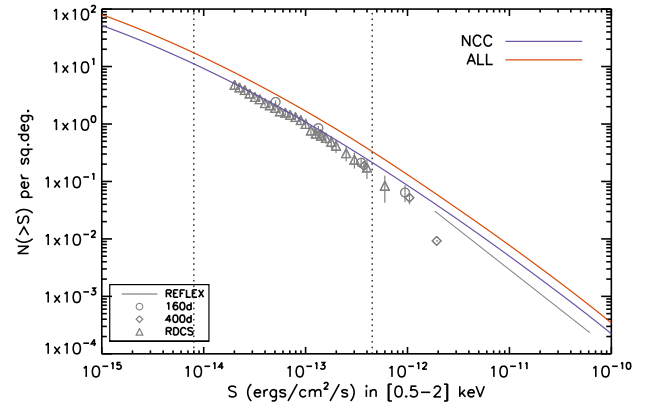
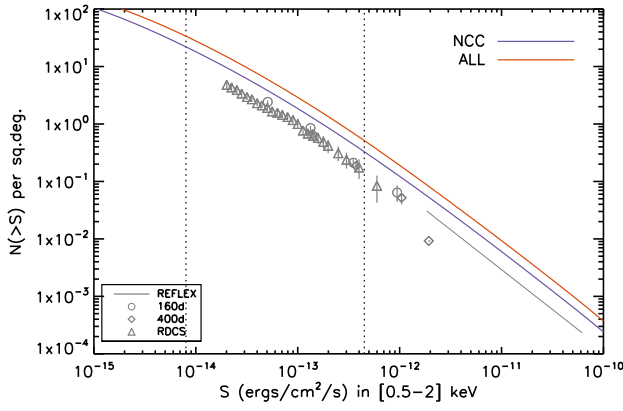


Figure 14. The cluster $\log N$ - $\log S$. The blue and red curves correspond to our predictions assuming the local ‘NCC’ and ‘ALL’ L–T relations respectively, both taken with $\sigma_{\ln L|T} = 0.7$ and are computed for the WMAP-5 cosmology. *Left panel:* Self-similar evolution is assumed for the scaling laws ($\gamma_{z,MT} = \gamma_{z,LT} = 0$). *Right panel:* Evolution as inferred from our 3-parameter best fit on the X-CLASS CR–HR distribution ($\gamma_{z,MT}$ and $\gamma_{z,LT}$, Table 7). Data points correspond to observations from various surveys (see text). The vertical lines indicate the approximate flux range of our sample.

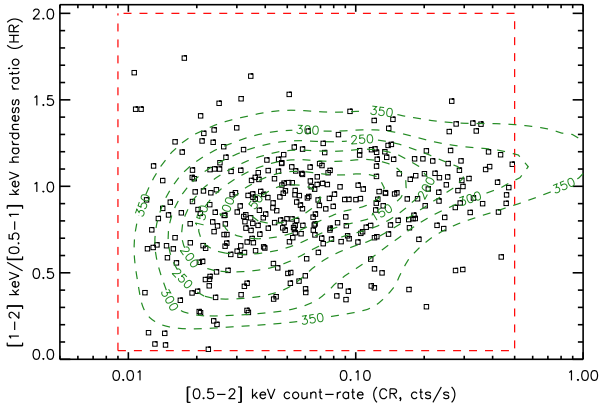


Figure 16. Best fit model (green dashed contours) overlaid on the CR–HR diagram data points. Five parameters are fitted assuming the local L–T relation from ‘NCC’ and $\sigma_{\ln L|T} = 0.7$. Contour labels indicate the predicted number of clusters enclosed by the corresponding contours. The red box shows the region in which the fit is performed. Measurement errors and bias due to pointed clusters have been included in the computation of the green contours.

HR diagram (assuming an average flux conversion factor of 9.10^{-13} ergs/s/cm² per cts/s). The high- and low-flux ends of this curve are not probed by our data points but rather rely on the validity of the assumed model, and in particular on the fact that scaling laws behave as Eqs. 2 and 3 at all redshifts. Such an extrapolation disagrees with REFLEX data points, as is the case in Fig. 14 where cosmological parameters are held at their WMAP value. Changes in the shape of scaling laws as a function of cluster properties and/or a disagreement between the different selection functions of various surveys may explain this discrepancy.

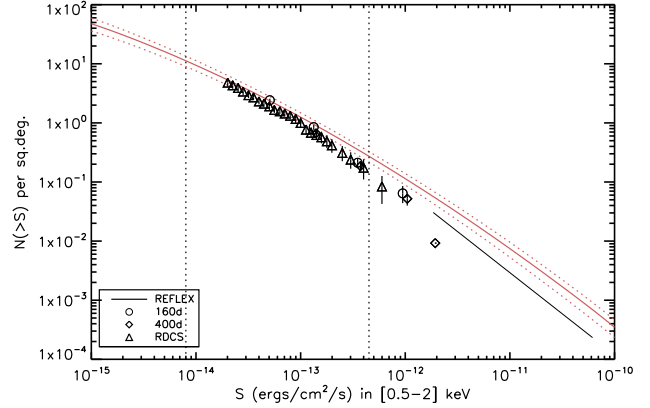


Figure 17. The cluster $\log N$ - $\log S$. The plain red curve shows the modeled distribution computed assuming the local L–T relation of ‘NCC’ with $\sigma_{\ln L|T} = 0.66$. Cosmological parameters as well as the non-similar evolution of scaling laws have been adjusted so as to match the CR–HR distribution of sources in the X-CLASS sample (best-fit parameters quoted in Sect. 5.2). The red dotted curves are computed by propagating the uncertainties on these parameters in the $\log N$ - $\log S$ computation. The vertical lines indicate the approximate flux range of our sample.

6 DISCUSSION

6.1 Cosmological parameters

Our analysis indicates values for Ω_m and σ_8 of 0.24 and 0.88 respectively with a $\sim 25\%$ and $\sim 15\%$ accuracy. These constraints are compatible with the most recent measurements from the CMB (Dunkley et al. 2009; Larson et al. 2011) and BAO observations (Percival et al. 2010; Blake et al. 2011). They are also in agreement with the most recent studies of X-ray selected clusters (Vikhlinin et al. 2009; Henry et al. 2009; Mantz et al. 2010a), Sunyaev-Zeldovich selected clusters (Vanderlinde et al. 2010; Sehgal et al. 2011) and optically selected clusters (Rozo et al. 2010).

Our results have been obtained for fixed local scaling

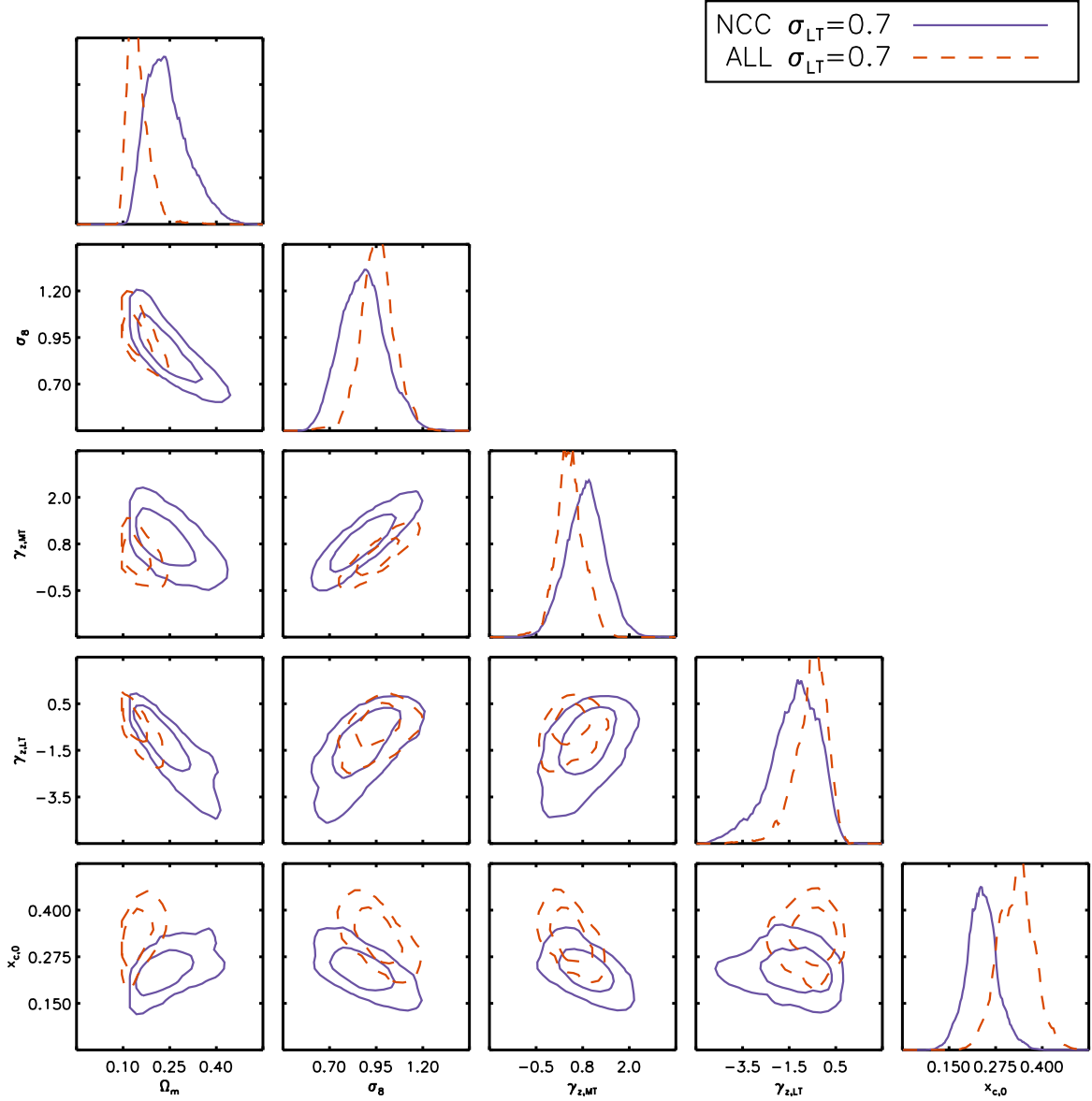


Figure 15. Posterior distribution for the five parameters fitted using the X-CLASS CR-HR distribution. The local L-T relation is ‘NCC’ or ‘ALL’ with a logarithmic dispersion $\sigma_{\ln L|T} = 0.7$. Diagonal panels represent the one-dimensional marginal distributions for each parameter (normalized to unit area), sub-diagonal panels show the two-dimensional contours enclosing 68% and 95% of the marginalized posterior distribution.

relations, in particular the ‘NCC’ L-T relation was taken from Pratt et al. (2009), with a constant logarithmic scatter of 0.7. We note that their relation has been derived for an assumed Λ CDM cosmology ($\Omega_m = 0.3, \Omega_\Lambda = 0.7, h = 0.70$) and strictly speaking it should be converted for each tested cosmology. However, we checked that the corresponding correction from $\Omega_m = 0.3$ to $\Omega_m = 0.24$ on the L-T normalisation amounts to less than 5% and thus neglected this correction in the analysis.

We checked that assuming the L-T relation from

Arnaud & Evrard (1999) (converted in the WMAP-5 cosmology) leads to compatible constraints on Ω_m and σ_8 . Interestingly, the ‘ALL’ ($\sigma_{\ln L|T} = 0.7$) from Pratt et al. (2009) predicts $\Omega_m = 0.15 \pm 0.04$ and $\sigma_8 = 0.96 \pm 0.08$, in disagreement with the other works cited above. Fig 15 compares the confidence contours obtained for both scaling relations and illustrates the marginal agreement of the posterior distributions. In all cases (‘NCC’, ‘ALL’ and Arnaud & Evrard 1999) we tested two different values for the intrinsic scatter $\sigma_{\ln L|T}$ (0.3 and 0.7) and noticed little change in the (Ω_m, σ_8)

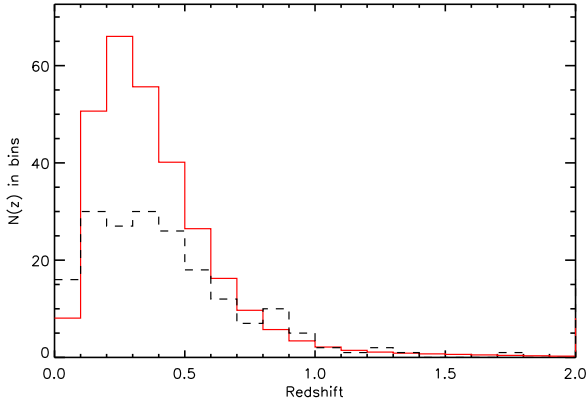


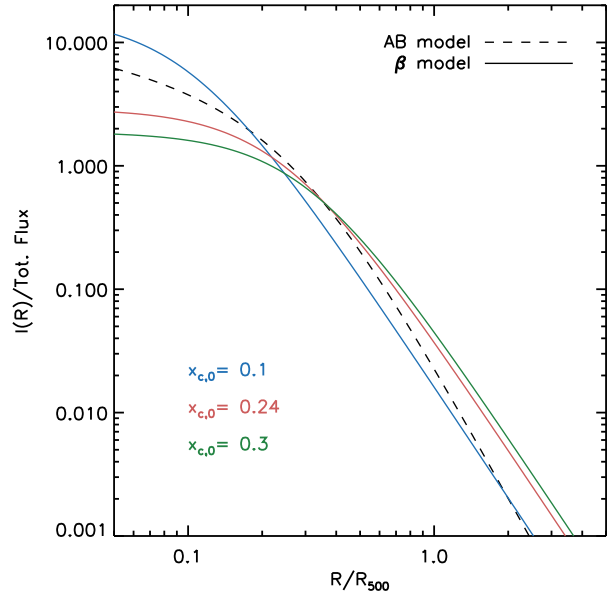
Figure 18. Predicted redshift distribution for the “C1+” clusters in the X-CLASS cosmological subsample (red solid histogram). The redshift distribution of clusters in our sample with known redshifts from the literature is indicated by the black dashed line.

constraints. This result is compatible with Sahlén et al. (2009) who find very little degeneracy between $\sigma_{\ln L|T}$ and cosmological parameters.

From the best set of parameters (Sect 5.2), we infer the redshift distribution of our cosmological cluster sample (Fig. 18) for the pure C1+ selection (with no bias from pointed clusters). It shows (*a posteriori*) that the distribution peaks around $z_{\text{med}} \sim 0.3 - 0.4$ with only 8.4 C1+ clusters beyond $z = 1$. The redshift histogram of clusters with known redshifts from the literature clearly illustrates the complexity of this bias in our sample. All sources in the first $0 < z < 0.1$ bin have a redshift, and there is a small excess of pointed clusters between $z = 0.8$ and $z = 1$. In total, 188 clusters out of the 347 ones selected for the CR–HR analysis have a redshift (66 of them being flagged as ‘tentative’ in our database, see Sect. A). However, including this partial redshift information in the MCMC analysis requires a precise knowledge of the associated selection process which is currently out of reach.

6.2 Cluster X-ray profiles

To account for the physical extent of clusters entering the survey selection function, we have introduced the $x_{c,0}$ parameter linking the X-ray cluster extent to the cluster mass ($x_{c,0} = r_c/R_{500c}$). Contrary to other studies, we did not assume a fixed physical size for the core radius (Pacaud et al. 2007; Sahlén et al. 2009) nor a size distribution (Burenin et al. 2007). In all configurations we investigated, this parameter is constrained at the 10 – 20% level and is found to have a value of 0.24 ± 0.04 in the best-fit model. For a cluster of mass $M_{200c} = 10^{14} h^{-1} M_{\odot}$ at redshift $z = 0.4$, R_{500c} is ~ 0.6 Mpc, and our result suggests a physical core radius of about 150 kpc, indeed typical of those found in other cluster studies at a similar redshift (e.g. Pacaud et al. 2007; Vikhlinin et al. 1998b; Burenin et al. 2007). As shown on Fig. 19, there is a reasonable agreement between a β -profile computed with our value of $x_{c,0}$ and the AB-model used in (Piffaretti et al. 2011), based on the local gas density profiles of the REXCESS clusters (Croston et al. 2008).



0

Figure 19. Comparison between the AB model from (Croston et al. 2008; Piffaretti et al. 2011) and the β -model used in this analysis ($\beta = 2/3$). These curves show surface brightness profiles normalized to the same total flux. The red curve corresponds to a β profile computed with the best-fit parameter $x_{c,0}$ from the MCMC analysis.

6.3 Scaling-laws evolution

We parametrised the redshift evolution of each scaling law by two factors of the form $(1+z)^\gamma$ such that $\gamma \neq 0$ indicates a departure from self-similar evolution (Equ. 2 and 3). The modelling of the CR–HR distribution includes self-consistently selection effects and the evolution of cluster scaling relations which is a key point of such analyses (e.g. Pacaud et al. 2007; Short et al. 2010; Mantz et al. 2010a).

We illustrate in Fig. 20 the net effect of the combined factors $E(z)$ and $(1+z)^\gamma$ in the evolution of scaling laws, using the best-fit values from our analysis. In this figure, the T–M relation has been computed by inverting Eq. 2 and is expressed in terms of the critical mass M_{200c} . The upper and lower boundaries have been computed using the covariance matrix of Ω_m (which enters $E(z)$), $\gamma_{z,MT}$ and $\gamma_{z,LT}$ output of our MCMC chain.

Our fit to the X-CLASS CR–HR diagram indicates a quasi non-evolving T– M_{200c} relation (equivalently, a negative evolution relative to the self-similar expectation), meaning that a cluster with a given mass M_{200c} shows approximately the same temperature at all redshifts. Our data also indicates a negative evolution of the L–T relation, below the self-similar expectation, a result that has been found in simulations of Kay et al. (2007) where feedback by AGN and stars is included in cluster simulations, and in Short et al. (2010) for their preheating model of cluster evolution. These trends are also observed by Ettori et al. (2004) for the M–T and L–T relations but are in conflict with studies from Kotov & Vikhlinin (e.g. 2005); Branchesi et al. (e.g. 2007). However, the comparison between these studies is hampered by the different selection processes entering different cluster

samples, which can have a tremendous effect on the derived evolution (Pacaud et al. 2007).

Finally, we note that our results do not firmly exclude self-similar evolution both in the M–T and the in L–T relations. The relatively large uncertainties on $\gamma_{z,MT}$ and $\gamma_{z,LT}$ are due to the absence of redshifts and to the degeneracies with cosmological parameters inherent to the CR–HR analysis (Fig. 15). We expect the forthcoming XXL and XCS surveys to provide tighter constraints on the evolution of scaling laws thanks to the inclusion of cluster redshifts in both analyses.

6.4 CR–HR outliers

Fig 16 shows the good agreement between our best-fit model and the CR–HR distribution of clusters in the sample. However, we note the presence of sources outside the bulk of the diagram. The top-left part³ ($CR < 0.06$, $HR > 1.4$) contains regular, weak clusters for which measurement errors are large, particularly on HR (Fig. 13). Such hardness ratios could be explained by, e.g. a high metallicity of the intra-cluster medium favoring emission from bright spectral lines. The bottom-right region⁴ ($CR > 0.1$, $HR < 0.7$) contains 9 clusters whose morphology appeared strongly peaked at the centre, hence indicating a significant AGN or cool-core contribution; the net effect is to increase our integrated CR and modify the HR, with respect to normal clusters. One outlier (xclass 1937) is a compact group (HCG 057, Hickson, Kindl, & Auman 1989) presenting a complex X-ray emission. A complete model would enclose cluster spectral peculiarities in the calculation of the CR–HR diagram; however, we consider here that their number is sufficiently low to neglect their impact onto our results.

6.5 Predictions for eRosita

In paper I, we presented Fisher forecasts for an XMM 100 sq. deg. cluster survey at a 10 ks depth, providing a sample of 570 clusters. The CR–HR method was predicted to yield the following accuracy: $\sigma(\Omega_m) = 0.09$, $\sigma(\sigma_8) = 0.14$, $\sigma(\gamma_{z,MT}) = 0.6$, $\sigma(\gamma_{z,LT}) = 2.3$ and $\sigma(x_{c,0}) = 0.04$. The present study has been conducted for similar conditions (comparable area, a somewhat more stringent selection function and partially deeper exposures). The good agreement between the predicted uncertainties and the output of the MCMC runs shows that both analyses are consistent with each other. We note however that there is not a one-to-one correspondence between them as the Fisher analysis involved more free parameters (though constrained with stringent priors) and there are 347 clusters in the present study, which are on average better measured than assumed in paper I. The difference in the total number of clusters is explained by: i) the more stringent selection function, ii) the actual 90 sq.deg. coverage of the X–CLASS survey, iii) inhomogeneities in the survey depth in terms of pointing background and hydrogen column density and iv) differences in

Table 8. Expected marginalized constraints on dark energy parameters and parameters describing the scaling-law evolution for the 20,000 sq.deg. eRosita survey. In each case, the scaling relations are let free in the analysis (slope, normalization and scatter). Planck priors are applied to the five parameters Ω_m , σ_8 , Ω_b , n_s and h .

	CR–HR		z–CR–HR	
	No prior	Planck priors	No prior	Planck priors
w_0	0.6	0.4	0.1	0.1
w_a	1.0	0.9	0.3	0.3
$\gamma_{z,MT}$	1.3	0.1	0.2	0.05
$\gamma_{z,LT}$	0.8	0.5	0.3	0.1

the fiducial parameters of the Fisher matrix and those derived in the present work (e.g. $x_{c,0} = 0.1$ in paper I and 0.2 in this paper).

The overall good agreement between predicted and measured uncertainties allows us to propose general predictions for the Rosita all-sky survey (Predehl et al. 2010) to be obtained by the CR–HR method, following the formalism developed in paper I. We assume a total area of 20,000 sq.deg. (extragalactic survey) and a custom selection function being a scaled-up version of the C1⁺ selection (Fig. 9). Within our fiducial model, the survey is expected to yield 2.5 clusters per sq.deg., hence a total of 50,000 detected clusters. In contrast to paper I, we do not assume priors on local scaling laws. We allow their normalization, slope and intrinsic scatter to vary, and let them evolve with redshift as $(1+z)^\gamma$. We assume a prior Fisher matrix on Ω_m , σ_8 , Ω_b , n_s and h as will be available from *Planck* and calculated identically as in Pierre et al. (2011) (based on the *Planck* mission definition – *Bluebook*⁵).

We estimate measurement errors by assuming a mean exposure time of 2.5 ks and an effective area equal to that of XMM MOS+PN (Predehl et al. 2010), thus applying a factor 2 to the uncertainties quoted in paper I for a 10 ks XMM survey. We considered two extreme situations: either no redshifts are available and we apply a simple CR–HR analysis, or all clusters do benefit from photometric redshifts and we use the more fruitful z–CR–HR analysis with bins of $\Delta z = 0.03$. Corresponding results are shown on Fig. 21 and quoted in Table 8, for the dark energy parameters (w_0 , w_a) and for the parameters governing the scaling-law evolution ($\gamma_{z,MT}$, $\gamma_{z,LT}$). We find that even without redshifts, the CR–HR method yields good constraints on the evolution of scaling laws, provided that the cosmological model is known at the accuracy expected from the Planck mission. The constraints on w_0 and w_a are less informative, but could be enhanced by a joint study of the angular correlation function of the detected clusters. In particular, we notice that adding Planck priors to the analysis has a mild impact on the dark energy constraints, possibly because of the degeneracies within the scaling-relation parameters and the relatively high uncertainties on the count-rate measurements. Adding redshift information considerably improves the expected constraints on both sets of parameters.

³ X–CLASS tags: 35, 86, 915, 997, 1032, 1655, 1741, 1886, 1947.

⁴ X–CLASS tags: 102, 238, 541, 1020, 1218, 1480, 1906, 1937, 2046, 2048, 2162, 2321.

⁵ <http://www.rssd.esa.int/index.php?project=Planck>

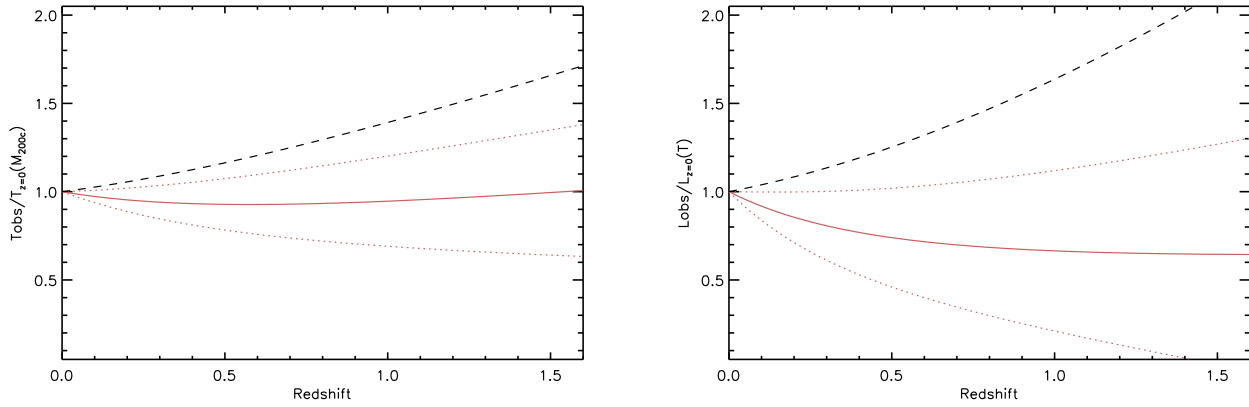


Figure 20. Scaling-law evolution as predicted by our model and parametrised by equations 2 and 3. The solid red line shows the best-fit model ($\Omega_m = 0.24$, $\gamma_{z,MT} = 0.8$, $\gamma_{z,LT} = -1.3$) with the dotted line indicating the 68% confidence boundaries. The black dashed line shows the self-similar expectation ($\gamma_{z,LT} = \gamma_{z,MT} = 0$).

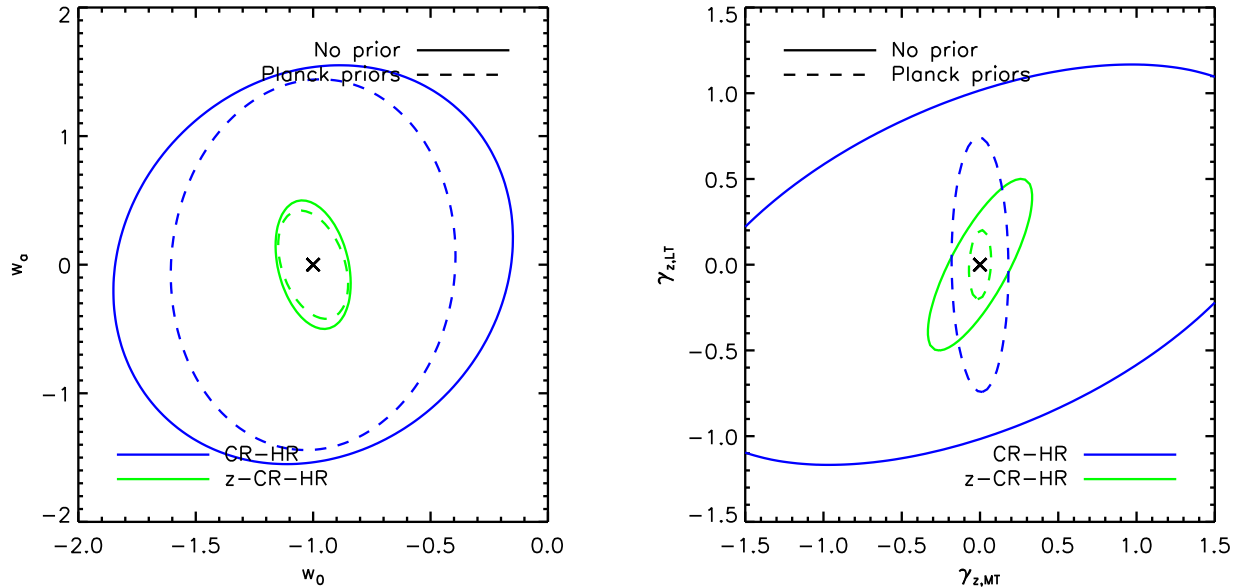


Figure 21. *Left:* constraints on the dark energy parameters w_0 and w_a for the eRosita 20000 sq.deg survey as predicted by the CR-HR method (blue), possibly supplemented by photometric redshifts for all clusters (z-CR-HR, green). No assumption has been made on scaling laws nor on their evolution and Planck priors were applied to Ω_m , σ_8 , Ω_b , n_s and h . The *right* panel shows the predicted constraints for cluster evolution

7 CONCLUSIONS AND PERSPECTIVES

We have presented the cosmological study of a sample of 347 clusters detected in the full *XMM-Newton* archive using X-ray criteria only (ancillary optical images were used to discard ‘extended’ sources irrelevant for our analysis such as nearby galaxies, saturated point-sources etc...). The study relies on the sole instrumental count-rates measured for each cluster in three X-ray bands. The selection function of our sample has been thoroughly defined by means of extensive image simulations and we proposed a method to account for the presence of pointed clusters in the analysis. We have then modeled the sample CR-HR diagram (whose properties are discussed in paper I) by self-consistently including

a Λ CDM cosmological model, X-ray scaling laws, selection effects and measurement errors. This allowed us to fit Ω_m and σ_8 along with the parametrized evolution of scaling laws plus a parameter $x_{c,0}$ characterizing the X-ray gas extent in clusters. We summarize below our main conclusions:

- When setting the cosmological parameters to their WMAP-5 values, we observe a preference for the ‘Non Cool Core’ normalization and slope of the L–T relation of Pratt et al. (2009), if we assume an intrinsic scatter of $\sigma_{lnL|T} \sim 0.7$. Our data then indicates a positive evolution of the M–T relation and a negative evolution of the L–T relation with respect to the self-similar expectation.
- Fitting Ω_m and σ_8 together with the evolution of scaling

laws, we still find a preference for the ‘NCC’ scaling law and find $\Omega_m = 0.24^{+0.04}_{-0.09}$ and $\sigma_8 = 0.88^{+0.10}_{-0.13}$, in agreement with the most recent cosmological studies. Again, the T–M and L–T scaling relations are found to evolve negatively with respect to the self-similar expectation.

- Assuming the ‘ALL’ scaling relation, our data indicates $\Omega_m \sim 0.15$ and $\sigma_8 \sim 0.96$ with a milder evolution of scaling laws.

- The ad hoc parameter $x_{c,0} = r_c/R_{500c}$ giving the X-ray extent as a function of cluster mass is found to be well constrained within our framework, with a best value of 0.24, compatible with individual cluster studies.

- The interpretation and use of the currently available local cluster scaling relations has proven one of the main hurdle of our study. Given that these relations do not agree with each other, it is probable that they have not been entirely corrected from the selection biases affecting the sample from which they are derived.

- The scatter in the scaling relations plays an important role in the cosmological analysis and is probably degenerate with the slope and normalisation of the relations. It is likely that the scaling relations will be reliably determined only with very large cluster samples along with the simultaneous fit of cosmology and selection effects. We stress that the CR–HR method is able to achieve this in a self-consistent manner, by-passing the tedious step that consists in determining individual cluster masses.

- As a logical follow-up of the present study, we propose predictions for the eRosita All-Sky survey. Assuming the Planck priors and letting all cluster scaling-law parameters free, we show that the z-CR–HR method will allow a determination of the equation of state of the dark energy at the level of stage IV of the DETF (Albrecht et al. 2006). In addition, the cluster scaling-law evolution will be well determined.

- The X-CLASS serendipitous cluster catalogue extracted from the XMM archival data is available online at: <http://xmm-lss.in2p3.fr:8080/l4sdb/>

ACKNOWLEDGEMENTS

The authors thank the anonymous referee whose useful comments and suggestions improved the quality of this paper. We acknowledge useful discussions with Gabriel Pratt, Kathy Romer, Martin Sahlén and Patrick Valageas. The results presented here are based on observations obtained with XMM-Newton, an ESA science mission with instruments and contributions directly funded by ESA Member States and NASA. The UK Schmidt Telescope was operated by the Royal Observatory Edinburgh, with funding from the UK Science and Engineering Research Council (later the UK Particle Physics and Astronomy Research Council), until 1988 June, and thereafter by the Anglo-Australian Observatory. The blue plates of the southern Sky Atlas and its Equatorial Extension (together known as the SERC-J), the near-IR plates (SERC-I), as well as the Equatorial Red (ER), and the Second Epoch [red] Survey (SES) were all taken with the UK Schmidt telescope at the AAO. This research has made use of the NASA/IPAC Extragalactic Database (NED) which is operated by the Jet Propulsion Laboratory, California Institute of Technology, under con-

tract with the National Aeronautics and Space Administration. The present study has been supported by a grant from the Centre National d’Etudes Spatiales. TS acknowledges support from the ESA PRODEX Programme “XMM-LSS”, from the Belgian Federal Science Policy Office and from the Communauté française de Belgique - Actions de recherche concertées. FP acknowledges support from Grant No. 50 OR 1003 of the Deutsches Zentrum für Luft- und Raumfahrt (DLR) and from the Transregio Programme TR33 of the Deutsche Forschungsgemeinschaft (DFG).

REFERENCES

- Adami C., Ulmer M. P., Romer A. K., Nichol R. C., Holden B. P., Pildis R. A., 2000, *ApJS*, 131, 391
- Albrecht A., et al., 2006, *astro*, arXiv:astro-ph/0609591
- Arnaud M., Evrard A. E., 1999, *MNRAS*, 305, 631
- Arnaud M., Pointecouteau E., Pratt G. W., 2005, *A&A*, 441, 893
- Arviset C., Dowson J., Hernández J., Osuna P., Venet A., 2003, *ASPC*, 295, 47
- Bertin E., Arnouts S., 1996, *A&AS*, 117, 393
- Blake C., et al., 2011, *MNRAS*, 415, 2892
- Böhringer H., et al., 2000, *ApJS*, 129, 435
- Böhringer H., et al., 2001, *A&A*, 369, 826
- Böhringer H., et al., 2004, *A&A*, 425, 367
- Borgani S., et al., 2001, *ApJ*, 561, 13
- Branchesi M., Gioia I. M., Fanti C., Fanti R., 2007, *A&A*, 472, 739
- Burenin R. A., Vikhlinin A., Hornstrup A., Ebeling H., Quintana H., Mescheryakov A., 2007, *ApJS*, 172, 561
- Cash W., 1979, *ApJ*, 228, 939
- Cavaliere A., Fusco-Femiano R., 1976, *A&A*, 49, 137
- Clerc N., Pierre M., Pacaud F., Sadibekova T., 2011, arXiv, arXiv:1109.4440
- Croston J. H., et al., 2008, *A&A*, 487, 431
- Dunkley J., et al., 2009, *ApJS*, 180, 306
- Eisenstein D. J., Hu W., 1998, *ApJ*, 496, 605
- Ettori S., Tozzi P., Borgani S., Rosati P., 2004, *A&A*, 417, 13
- Henry J. P., Evrard A. E., Hoekstra H., Babul A., Mahdavi A., 2009, *ApJ*, 691, 1307
- Hickson P., Kindl E., Auman J. R., 1989, *ApJS*, 70, 687
- Jones C., Forman W., 1999, *ApJ*, 511, 65
- Jones L. R., Scharf C., Ebeling H., Perlman E., Wegner G., Malkan M., Horner D., 1998, *ApJ*, 495, 100
- Kalberla P. M. W., Burton W. B., Hartmann D., Arnal E. M., Bajaja E., Morras R., Pöppel W. G. L., 2005, *A&A*, 440, 775
- Kay S. T., da Silva A. C., Aghanim N., Blanchard A., Lidde A. R., Puget J.-L., Sadat R., Thomas P. A., 2007, *MNRAS*, 377, 317
- Kolokotronis V., Georgakakis A., Basilakos S., Kitsionas S., Plionis M., Georgantopoulos I., Gaga T., 2006, *MNRAS*, 366, 163
- Kotov O., Vikhlinin A., 2005, *ApJ*, 633, 781
- Larson D., et al., 2011, *ApJS*, 192, 16
- Lloyd-Davies E. J., et al., 2011, *MNRAS*, 418, 14
- Mantz A., Allen S. W., Rapetti D., Ebeling H., 2010, *MNRAS*, 406, 1759

Mantz A., Allen S. W., Ebeling H., Rapetti D., Drlica-Wagner A., 2010, MNRAS, 406, 1773

Maughan B. J., Giles P. A., Randall S. W., Jones C., Forman W. R., 2012, MNRAS, 2419

Mehrtens N., et al., 2011, arXiv, arXiv:1106.3056

Mittal R., Hicks A., Reiprich T. H., Jaritz V., 2011, A&A, 532, A133

Moretti A., Campana S., Lazzati D., Tagliaferri G., 2003, ApJ, 588, 696

Pacaud F., et al., 2006, MNRAS, 372, 578

Pacaud F., et al., 2007, MNRAS, 382, 1289

Percival W. J., et al., 2010, MNRAS, 401, 2148

Peterson J. R., Jernigan J. G., Gupta R. R., Bankert J., Kahn S. M., 2009, ApJ, 707, 878

Pierre M., et al., 2007, MNRAS, 382, 279

Pierre M., Pacaud F., Juin J. B., Melin J. B., Valageas P., Clerc N., Corasaniti P. S., 2011, MNRAS, 414, 1732

Piffaretti R., Arnaud M., Pratt G. W., Pointecouteau E., Melin J.-B., 2011, A&A, 534, A109

Pratt G. W., Croston J. H., Arnaud M., Böhringer H., 2009, A&A, 498, 361

Predehl P., et al., 2010, SPIE, 7732,

Read A. M., Ponman T. J., 2003, A&A, 409, 395

Reid I. N., et al., 1991, PASP, 103, 661

Romer A. K., et al., 2000, ApJS, 126, 209

Romer A. K., Viana P. T. P., Liddle A. R., Mann R. G., 2001, ApJ, 547, 594

Rosati P., della Ceca R., Norman C., Giacconi R., 1998, ApJ, 492, L21

Rozo E., et al., 2010, ApJ, 708, 645

Sahlén M., et al., 2009, MNRAS, 397, 577

Scharf C. A., Jones L. R., Ebeling H., Perlmutter E., Malkan M., Wegner G., 1997, ApJ, 477, 79

Sehgal N., et al., 2011, ApJ, 732, 44

Short C. J., Thomas P. A., Young O. E., Pearce F. R., Jenkins A., Muanwong O., 2010, MNRAS, 408, 2213

Smith B. J., 2007, J Stat Softw, 21, 1–37

Starck J.-L., Murtagh F. D., Bijaoui A., 1998, Image Processing and Data Analysis: The Multiscale Approach, Cambridge University Press, Cambridge (GB).

Takey A., Schwöpe A., Lamer G., 2011, A&A, 534, A120

Tinker J., Kravtsov A. V., Klypin A., Abazajian K., Warren M., Yepes G., Gottlöber S., Holz D. E., 2008, ApJ, 688, 709

Valtchanov I., Pierre M., Gastaud R., 2001, A&A, 370, 689

Vanderlinde K., et al., 2010, ApJ, 722, 1180

Vikhlinin A., McNamara B. R., Forman W., Jones C., Quintana H., Hornstrup A., 1998, ApJ, 502, 558

Vikhlinin A., McNamara B. R., Forman W., Jones C., Quintana H., Hornstrup A., 1998, ApJ, 498, L21

Vikhlinin A., et al., 2009, ApJ, 692, 1060

APPENDIX A: X-CLASS CATALOGUE

A1 Database

The X-CLASS catalogue is accessible through a dedicated database at <http://xmm-iss.in2p3.fr:8080/l4sdb/>

It contains 845 C1 clusters retained after data screening, in particular the 347 clusters used in the cosmological analysis. The public part of the database contains 422 clusters

selected identically as the cosmological sample (C1⁺, with high- and low-cuts in [0.5–2] keV count-rate and hardness-ratio, see Sect. 3) but extended up to 13 arcmin off-axis distance (instead of 10 arcmin). Redshifts were obtained from the NED and from the recent publication by Mehrrens et al. (2011) for the XCS survey.

We describe below the informations contained in the database:

- **Object name:** each cluster is referenced with a unique identifier (“tag”), a full name in the XMM-Newton format (XMMUJ) and a name output of the X-ray pipeline. The cluster name encloses the corresponding XMM ObsId (ex: 0502430101) and truncated exposure time (10ks or 20ks) at which it has been detected.

- **Object position:** the position of the cluster (right ascension and declination) as provided by the pipeline is given in addition to the position measured by hand in the course of the cluster count-rate measurement (Sect. 2.4).

- **NED identifications:** column ‘NED’ lists all sources (galaxies, galaxy clusters, groups, QSO, etc.) within 3 arcmin of the cluster centre having a redshift indication from the NED (photometric or spectroscopic). An illustrative example is given in Table A1.

- **Redshift:** when a redshift indication is available, we provide a flag describing the current status of the redshift determination: ‘confirmed’ for a cluster definitely confirmed, ‘tentative’ if less than 3 concordant redshifts within 3 arcmin are available and ‘photometric’. Redshifts are quoted from NED first, then from the XCS-DR1 taking into account the provided flags.

- **X-ray properties:** basic X-ray properties output of the XAmin pipeline (Sect. 2.2) are given for each cluster, in the [0.5–2] keV detection band: number of counts, total count-rate, apparent Extent and Extent Likelihood as well as the distance to the centre of the pointing it belongs to (off-axis).

- **Count-rates:** count-rates measured manually in several energy bands are also available, in particular for the [0.5–2] keV band. In any case, count-rates are specified ‘on-axis’, i.e. corrected from the local exposure map, and do not include the filter and aperture corrections as discussed in Sect. 2.4. A webpage shows for each cluster the profiles generated for the count-rate measurement (see Fig. A1 for a particular example).

- **Cluster images:** X-ray photon images, filtered images and optical cut-outs from the Palomar Observatory Sky Survey (POSS-II, Reid et al. 1991) have been produced and linked to each catalogue entry. A screenshot image is shown on Fig. A2.

- **Database interface:** the electronic catalogue can be sorted according to any of entry of the database and can be downloaded as a machine-readable file.

A2 Comparison to the XCS survey

We compared our catalogue to the first release of the XCS survey XCS-DR1 (Mehrtens et al. 2011) based on the analysis of all publicly available data in the XMM archive. For this comparison, we included our 347 clusters selected for the cosmological analysis (with off-axis distance below 10 arcmin)

Cluster candidate : 0201090401_17_v3.3_c1_10ks id : 908

Xray Overlays

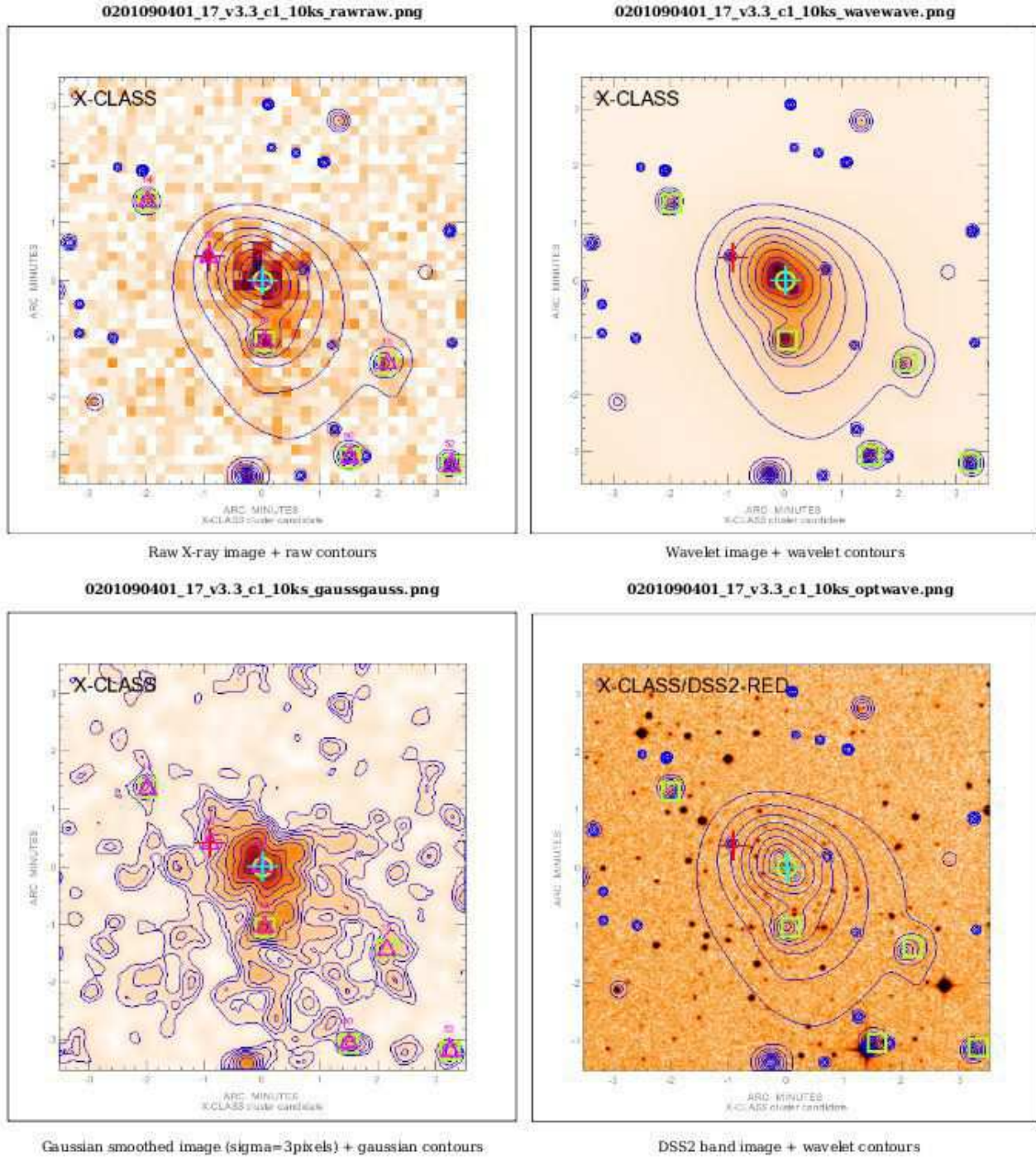


Figure A2. Screenshot of a webpage from the X-CLASS database (<http://xmm-lss.in2p3.fr:8080/l4sdb/>), for a particular cluster (tag 908). Displayed are the X-ray photon image (*top-left*) with associated contours, the wavelet-filtered (*top-right*) and gaussian-filtered (*bottom-left*) images and the optical (POSS-II) overlay (*bottom-right*).

Table A1. Sample table attached to the ‘NED’ column in the database, for a particular cluster (tag 1758). This table lists all objects from the Nasa Extragalactic Database (April 2011) within 3 arcmin of the cluster center, with an associated redshift. Values in the table are directly copied from the NED and originate from various surveys/follow-ups. In particular, the redshift accuracy is highly inhomogeneous and in some cases a flag indicates its reliability. The velocity of each object is expressed in km/s. The distance is quoted relative to the cluster centre (units arcmin).

N	Name	R.A.	Dec	Type	Velocity	Redshift	Z flag	Magnitude	Distance
1	2MASX J10531862+5720438	163.32800	57.34570	G	101956	0.34009		20.3g	0.0
2	SL J1053.4+5720	163.32700	57.34640	GClstr	101929	0.34			0.1
3	SHADES J105319+572110	163.33000	57.35280	G	779460	2.6	PHOT		0.4
4	1EX 179	163.32899	57.36120	G	39872	0.133		17.1R	1.0
5	SDSS J105318.96+572140.5	163.32899	57.36130	G	39911	0.133		17.9g	1.0
6	[MBC2005] 0086	163.28999	57.34990	G	1025290	3.42			1.3
7	SDSS J105329.42+572104.2	163.37300	57.35120	QSO	343262	1.145		21.3	1.5
8	SDSS J105319.03+571851.8	163.32899	57.31440	G	213152	0.711		21.3g	1.9
9	SDSS J105328.81+572205.1	163.37000	57.36810	G	232639	0.776		23.5g	1.9
10	SDSS J105319.99+572251.1	163.33299	57.38090	G	158290	0.528		22.6g	2.1
11	[ZMF2005] 007	163.37601	57.37820	G	258721	0.863			2.5
12	SDSS J105311.65+572305.6	163.29900	57.38490	G	462880	1.544		23.2	2.6
13	SDSS J105330.86+572247.6	163.37900	57.37990	G	190068	0.634		23.3g	2.6
14	[ZMF2005] 006	163.38800	57.37640	G	220347	0.735			2.7
15	[ZMF2005] 005	163.40199	57.37150	G	144500	0.482			2.8
16	Bolocam LE 1100.01	163.23801	57.35080	G	929357	3.1	PHOT	26.14	3.0

plus 75 clusters selected upon identical criteria, but with off-axis distances between 10 and 13 arcmin (thus 422 clusters in total). The XCS-DR1 sample is composed of 503 clusters which are optically confirmed and detected with more than 300 counts in the [0.5-2] keV band. Clusters identified as targets of a particular XMM observation are not included in the XCS-DR1. Fig. A3 illustrates the comparison between the two samples. Out of our 422 clusters, 159 are new discoveries (i.e. not in the XCS-DR1 and without information from NED). The differences between the two catalogues can be attributed to the different pointing selection and to differences in the X-ray detection algorithms. A further comparison between the two analyses will provide useful insights into the different selection effects and possible systematics contained in both samples.

APPENDIX B: BIAS CORRECTION FOR POINTED OBSERVATIONS

We detail in this Appendix our method for correcting from the presence of pointed clusters in the XMM archive. As shown on Figures 10 and 11, more clusters are detected in the inner 5 arcmin than expected from solely considering the sensitivity gradient on the detectors. This sensitivity difference is partly due to the EPIC vignetting function (loss of $\sim 60\%$ in effective area at 10 arcmin off-axis (“XMM-Newton Users Handbook”, Issue 2.9, 2011 (ESA: XMM-Newton SOC)) compared to the centre). The degradation of the telescope PSF at larger off-axis distances is the second most important cause of sensitivity variation as it dilutes the signal of faint sources and distorts their shape.

B1 Bias model

We want to correct the CR–HR distribution from the bias due to pointed clusters, directly on the predicted CR–HR

distribution. We assume that this correction does not depend on HR and divide the count-rate distribution in several bins indexed by j . We call n_j the underlying cluster surface density, i.e. the value obtained after integrating the true cluster $\log(N)$ -log(CR) in bin j . We introduce the survey selection function through the factor ϵ_j (comprised between 0 and 1) such that the net number of clusters detected in bin j for an arbitrary region covering $A = \Omega f_{sky}$ sr. on sky is:

$$N_j^{\text{tot}} = A \epsilon_j n_j \quad (\text{B1})$$

Here the sky area is $\Omega = 4\pi(1 - \cos 70^\circ)$ as we exclude the galactic plane ($\pm 20^\circ$) from the analysis.

We now divide the survey in two sub-surveys labelled ‘in’ and ‘out’. The first one gathers all regions belonging to the inner [0-5] arcmin and the latter corresponds to the [5-10] arcmin regions of the same pointings. The total area covered by the survey reads $A = A^{\text{in}} + A^{\text{out}}$. Introducing μ_j^{in} (≥ 1) the sensitivity of the inner sub-survey relative to the total survey we write (still for an unbiased sample):

$$N_j^{\text{in}} = A^{\text{in}} \epsilon_j \mu_j^{\text{in}} n_j$$

We now consider that an unknown fraction f_j of all existing clusters on sky has been observed and pointed in the central region of the detectors, thus augmenting N_j^{in} by a quantity:

$$N_j^{\text{in,pointed}} = \Omega n_j f_j \epsilon_j \mu_j^{\text{in}}$$

Because those clusters have been removed from the sky population of clusters, the remaining density on sky is $n'_j = (1 - f_j) n_j$ and the survey provides a total number of clusters:

$$\begin{aligned} N_j^{\text{tot,biasd}} &= N_j^{\text{in,pointed}} + A \epsilon_j n'_j \\ &= \Omega n_j f_j \epsilon_j \mu_j^{\text{in}} + A \epsilon_j (1 - f_j) n_j \\ &= \left(\frac{1}{f_{sky}} f_j \mu_j^{\text{in}} + (1 - f_j) \right) N_j^{\text{tot}} \end{aligned} \quad (\text{B2})$$

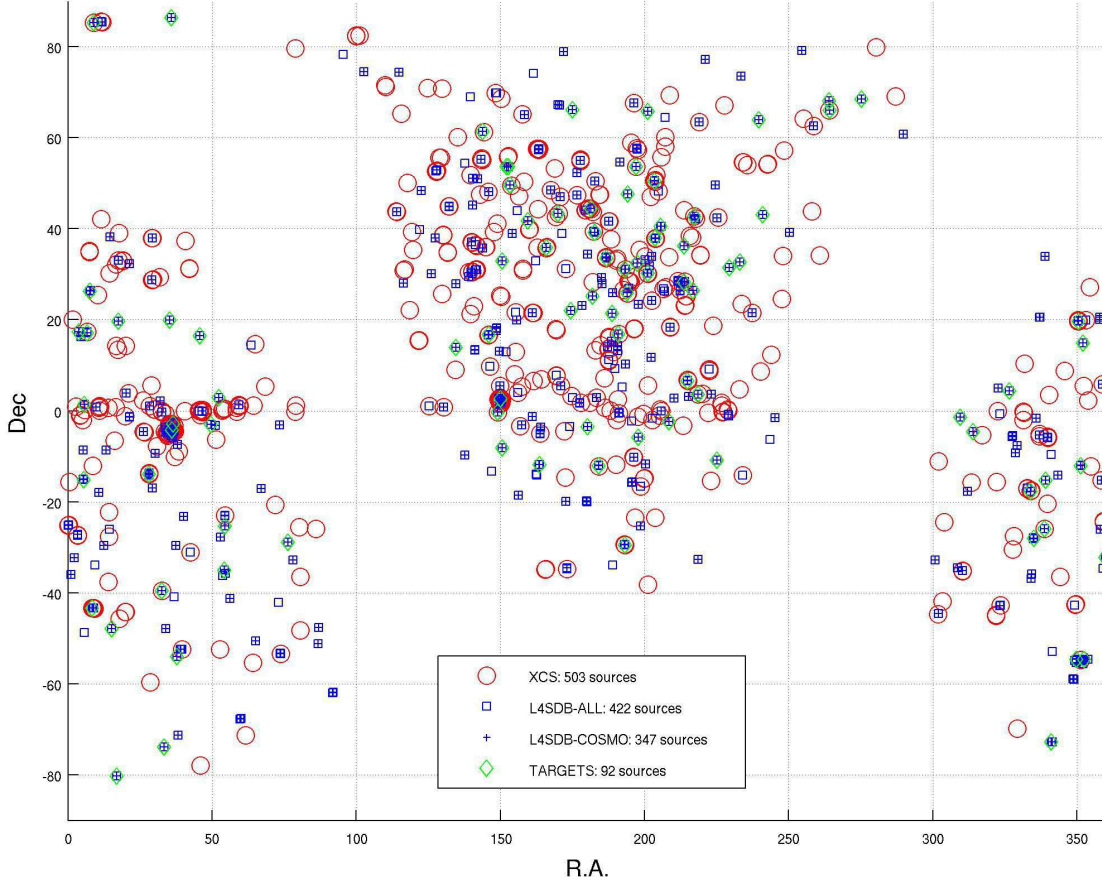


Figure A3. Comparison between the X-CLASS and the XCS-DR1 (Mehrtens et al. 2011) catalogues. Blue crosses stand for the cluster sample used in the cosmological analysis, blue squares for the “extended” cosmological sample (i.e. up to 13 arcmin off-axis distance on the XMM detectors). Green diamonds show the 92 sources of our sample located at the centre of the XMM field of view (i.e. less than 3 arcmin off-axis distance).

Comparing equations B1 and B2 we obtain the bias factor:

$$F_j = N_j^{\text{tot,biased}} / N_j^{\text{tot}} = \frac{1}{f_{sky}} f_j \mu_j^{\text{in}} + (1 - f_j) \quad (\text{B3})$$

B2 Bias estimation

Following previous equations, the expected number of clusters in the ‘in’ survey writes:

$$\begin{aligned} N_j^{\text{in,biased}} &= \Omega n_j f_j \epsilon_j \mu_j^{\text{in}} + A^{\text{in}} \epsilon_j \mu_j^{\text{in}} n'_j \\ &= \left[\frac{1}{f_{sky}} f_j + (1 - f_j) \frac{A^{\text{in}}}{A} \right] \mu_j^{\text{in}} N_j^{\text{tot}} \end{aligned} \quad (\text{B4})$$

while the expected number of clusters in the ‘out’ survey is:

$$N_j^{\text{out,biased}} = (1 - f_j) \left[1 - \mu_j^{\text{in}} \frac{A^{\text{in}}}{A} \right] N_j^{\text{tot}} \quad (\text{B5})$$

At this point, only two quantities are unknown, f_j and N_j^{tot} . Parameters A and A^{in} directly come from the survey geometric design. The factor μ_j^{in} is obtained by comparing the results of the simulations (Sect. 3) for clusters in the

full [0-10] arcmin off-axis area and for clusters in the central [0-5] arcmin region.

We compute independently in each bin the joint likelihood for the observed (biased) quantities $\widehat{N}_j^{\text{out}}$ and $\widehat{N}_j^{\text{in}}$ on a fine bidimensional grid sampling values for f_j and N_j^{tot} . We then compute the marginalized probability distribution $P(f_j)$ assuming flat priors for N_j^{tot} by numerical integration of the sampled likelihood.

The expectation value and variance for F_j are finally derived by integrating Eq. B3 against $P(f_j)$ and are displayed on Figure 12 for the present sample. The predicted, unbiased CR–HR distribution is multiplied by the expectation value of F_j linearly interpolated at each CR value.

This model relies on the hypothesis that all pointed clusters are centered onto the detectors. It thus neglects spatial correlation effects which may artificially boost the number of clusters in the surroundings of pointed clusters, in particular in the outer parts of the detectors.

This paper has been typeset from a \LaTeX file prepared by the author.

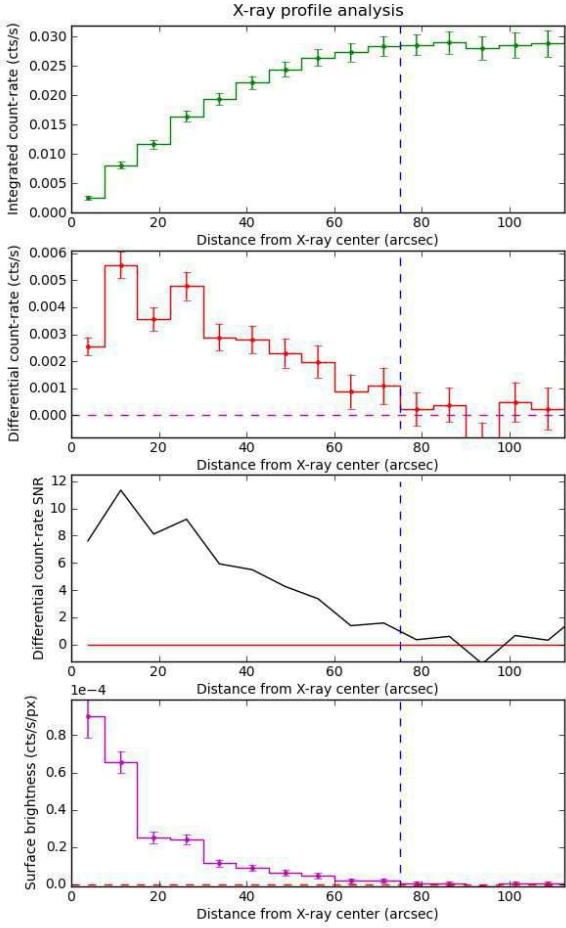


Figure A1. Screenshot of a webpage from the X-CLASS database (<http://xmm-lss.in2p3.fr:8080/l4sdb/>), for a particular cluster (tag 2094). Displayed are the cumulative, background-subtracted, count-rate profile (*top*) the differential count-rate profile (*2nd panel*), the corresponding signal-to-noise curve (*3rd panel*) and the surface brightness profile (*bottom*). The blue vertical lines shows the radius in which the measurement is performed.